Modeling the Proterozoic basement's effective stress field, assessing fault reactivation potential related to increased fluid pressures in south central Kansas and north central Oklahoma, and improving seismic imaging of basement faulting within Wellington and Anson-Bates Fields, Sumner County, Kansas

by

Ryan Taylor Keast

B.S., Kansas State University, 2016

A THESIS

submitted in partial fulfillment of the requirements for the degree

MASTER OF SCIENCE

Department of Geology
College of Arts and Sciences

KANSAS STATE UNIVERSITY
Manhattan, Kansas

2018

Approved by:

Co-Major Professor
Dr. Brice Lacroix

Approved by:

Co-Major Professor
Dr. Abdelmoneam Raef

Copyright

Abstract

South-central Kansas has experienced an increase in seismic activity within the Proterozoic basement over the past 10 years. In 2009, Oklahoma seismic stations recorded 50 earthquakes statewide, a 200% increase from 2008. Oklahoma Geological Survey (OGS) seismograph stations recorded 1,028 in 2010, an increase of over 2000% from 2009. Between 2000-2012, Kansas experienced only 12 earthquakes statewide. Beginning in September 2013, clusters of seismic events in south-central Kansas began to increase. In 2015 alone, Kansas seismograph stations recorded 448 earthquakes, of which 166 resulted in a magnitude 2.0 or greater. Since 2013, United States Geological Survey (USGS) seismograph stations have recorded over 12,000 earthquakes within Kansas and Oklahoma. Pore fluid pressure increases associated with recent high-rate wastewater injection into the dolomitic Arbuckle disposal zone are hypothesized as cause of reactivation of the faulted study region's Proterozoic basement. Although the magnitude of fluid-pressure change required for reactivation of these faults is likely low given failure equilibrium conditions in the midcontinent, heterogeneities (i.e. permeability, porosity, fluid pressure) in the basement could allow for a range of fluid pressure changes associated with injection. This research aims to quantify the fluid pressure changes responsible for fault reactivation of the Proterozoic basement. To address this issue, we use 97 earthquake focal mechanisms and over 12,000 seismic events, from the USGS catalog, within an area encompassing ~ 4,000 km^2. Focal mechanism data was utilized to determine the regional stress field present within the study region. Nodal plane data extracted from the focal mechanisms was crucial to identifying lineaments within the underlying basement complex.

A 3D seismic dataset covering the Wellington and Anson Bates Fields in north central Sumner County, Kansas was utilized for enhanced structural delineation of an interpreted fault

network affecting the Mississippian and Arbuckle Groups, to investigate whether it impacts the underlying granitic basement and its complex network of potentially interconnected fault planes. Smoothed similarity and spectral whitening analyses were applied to the dataset to improve depth of investigation and uncover fault lineaments masked by seismic attenuation due to increasing depth. An interpreted network of fault planes at depths of 3.5 km was uncovered beneath Wellington Field. The lineaments are well aligned with known structural features present within the Proterozoic basement, the Central Kansas Uplift and the Nemaha Ridge-Humboldt fault zone.

Table of Contents

List of Figures

List of Tables

Acknowledgements

Special thanks to Brice Lacroix, Abdelmoneam Raef, Claudia Adam, Matthew Totten, Tandis Bidgoli, Henri Leclere, and Guillaume Daniel for their assistance and expert advice regarding my research project. The level of knowledge each of you possess is humbling to say the least and an integral part of my success. It has been a pleasure working with you all. I am forever a better geoscientist because of your individual time, effort, guidance, and patience. I would also like to thank Helen and Brice Lacroix's family, Marie and Pierre, for graciously allowing me into their home in France this summer. Your family made me feel right at home and displayed generosity far beyond expectations. I cannot stress enough how thankful I am for their level of kindness. A special thanks to the Kansas State Geology Department Graduate Committee for accepting my application and generously offering me a Graduate Teaching Assistantship. I thoroughly enjoyed teaching young geoscientists and foresee a future career as a geoscience educator following industry-related experience.

Chapter 1 - Introduction

1.1. Background

South central Kansas and north central Oklahoma are home to extensive oil and gas production operations, high-volume wastewater disposal wells, and frequent seismic events uncommon prior to 2013 (Kansas Geological Survey (KGS): Kansas Earthquakes, Oklahoma Geological Survey Earthquake Catalog, 2018). Sumner County lies approximately 32 km south of Kansas' largest metropolitan area, Wichita, and shares its southern border with Grant and Kay Counties of Oklahoma. Grant County has consistently been one of the most seismically active counties in Oklahoma since 2009 when significant increases in the frequency and magnitude of seismicity were observed within the state (Oklahoma Geological Survey (OGS) Earthquake Catalog, 2018). In 2009, Oklahoma seismic stations recorded 50 earthquakes statewide, a 200% increase from 2008. Oklahoma Geological Survey (OGS) seismograph stations recorded 1,028 events in 2010, an increase of over 2000% from 2009 (OGS: Earthquake Catalog, 2018). Harper County, Kansas, west of Sumner County, over the past 4 years has recorded seismicity at an all-time high since extensive earthquake monitoring began. High rate salt water injection wells are prominent in the south central region of Harper County where a clear majority of the seismic activity has taken place.

Between 2000-2012, Kansas experienced only 12 earthquakes statewide. Beginning in September 2013, clusters of seismic events in south-central Kansas began to appear and have steadily increased. In 2015 alone, Kansas seismograph stations recorded 448 earthquakes, of which 166 registered as a magnitude 2.0 or greater (KGS: Kansas Earthquakes, 2018). In south-central Kansas, several small earthquakes were recorded near disposal wells in September 2013, approximately three years after horizontal drilling activities in the Mississippian limestone play and associated saltwater disposal had crossed over the state line into southern Kansas from northern Oklahoma (Buchanan et al., 2014). Previous studies within Oklahoma have investigated the increases in the volume of waste fluid injected and the associated seismic rate changes (Walsh and Zoback, 2015), (Figure 1). In total, Oklahoma and Kansas seismograph stations have recorded over 12,000 seismic events greater than magnitude 1.0 since 2009.

Seismic activity has decreased in 2016 due in part to orders and limitations imposed by the Kansas Corporation Commission (KCC) in March of 2015 (Peterie et al., 2015) These regulations have reduced the allowable daily barrel limits on wastewater disposal wells that inject into the Arbuckle Group and Mississippian Series disposal zones (Green, 2016), (Figure 2). The restrictions passed imposed by the KCC required that all injection wells disposing into the granitic Proterozoic basement, despite their rate of injection, cease injection operations immediately and be plugged-back and abandoned. The daily allowable rate for most Class I injection wells was 30,000 barrels a day prior to restrictions imposed by the KCC. Class I wells are used to inject hazardous wastes or dispose of industrial and municipal fluids beneath the lowermost formation containing, within one quarter (1/4) mile of the well bore, a source of fresh or usable water (KCC: Underground Injection Control Program (UICP), 2015). Class II wells are used to inject fluids associated with the production of oil and natural gas or fluids/compounds used for enhanced hydrocarbon recovery. These wells normally inject below the lower-most fresh or usable water bearing zone except in cases where this zone is hydrocarbon producing. These wells are regulated by the Kansas Corporation Commission (KCC: UICP, 2015). The greatest increase in seismicity has occurred near high-volume saltwater injection wells where allowable injection rates for 23 wells exceeded 30,000 barrels a day or more (KCC: UICP, 2015). The restrictions required all wells within 10 days of the order, to limit their injection rate to 16,000 barrels a day with a maximum allowable limit of 8,000 barrels a day within 100 days of the March 2015 executive order. There are 47 Class I injection wells located in Kansas, 46 of those dispose fluids into the heterogenous dolomitic Arbuckle disposal reservoir (KCC: UICP, 2015). A majority of the wastewater injected into the Arbuckle disposal zone is from oil and gas production, but petroleum refining, chemical production, commercial disposal, and municipal wastewater treatment operations all utilize the disposal zone for their unwanted byproducts (KDHE: UIC, 2018).

The aim of this research is to establish the theoretical pore fluid pressures required to reactivate Proterozoic basement faults based on their orientation, depth of burial, and the active regional stress field. Earthquake focal mechanisms generated from seismic waveform data indicate the type of faulting and the orientation of the fault plane. Fault planes will classified based on their orientation with the regional stress tensor and effective pore fluid pressures will be quantified utilizing this information. Very little research has been done in the study area where seismic activity has increased and high rate injection wells are present.

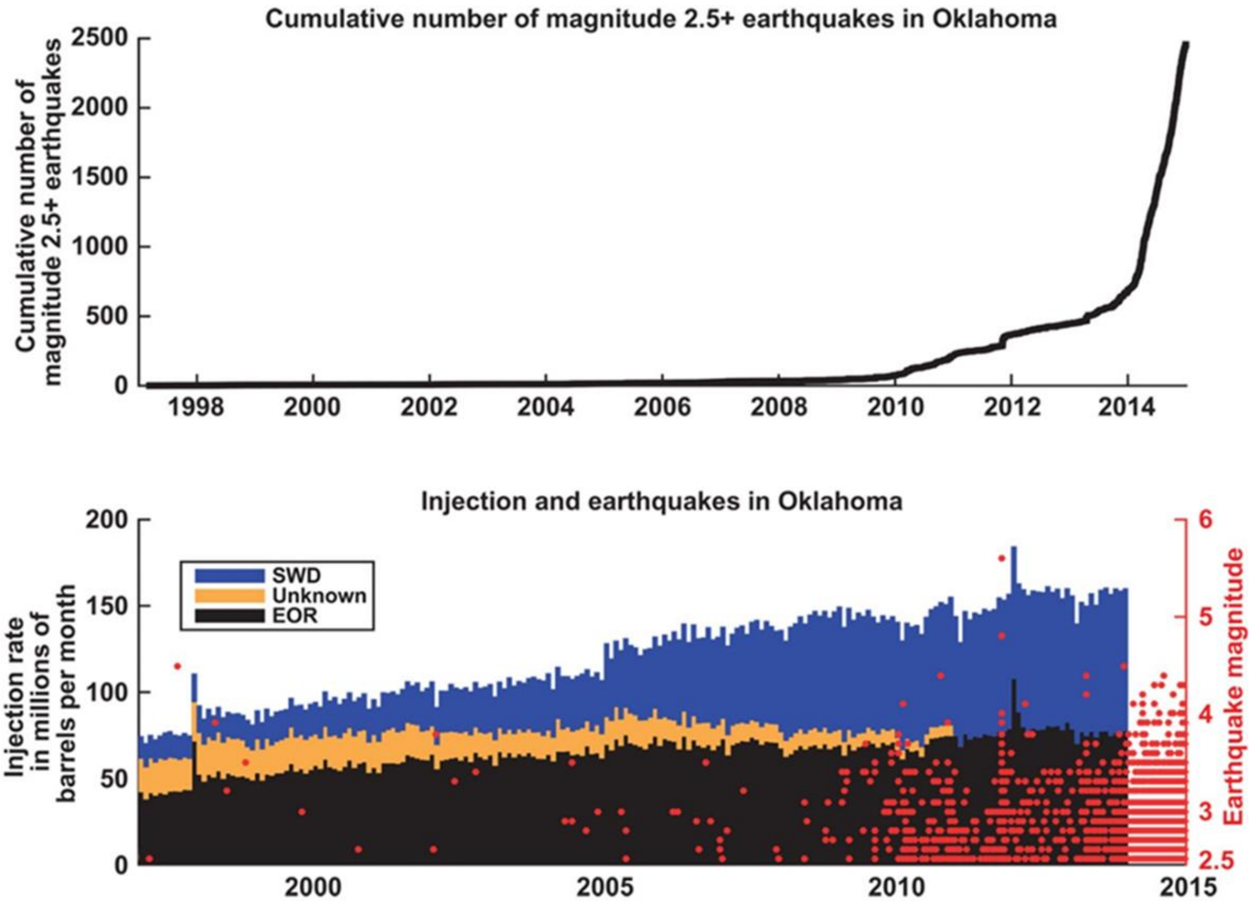

Figure 1: The increase in earthquake frequency in Oklahoma coincides with higher rates of salt water disposal (SWD). Enhanced Oil Recovery (EOR) rates have changed very little over the past 20 years. By comparison, SWD has increased by over 400% in that same amount of time. Since late 2013, Kansas has recorded a drastic increase in seismic activity (Walsh and Zoback, 2015).

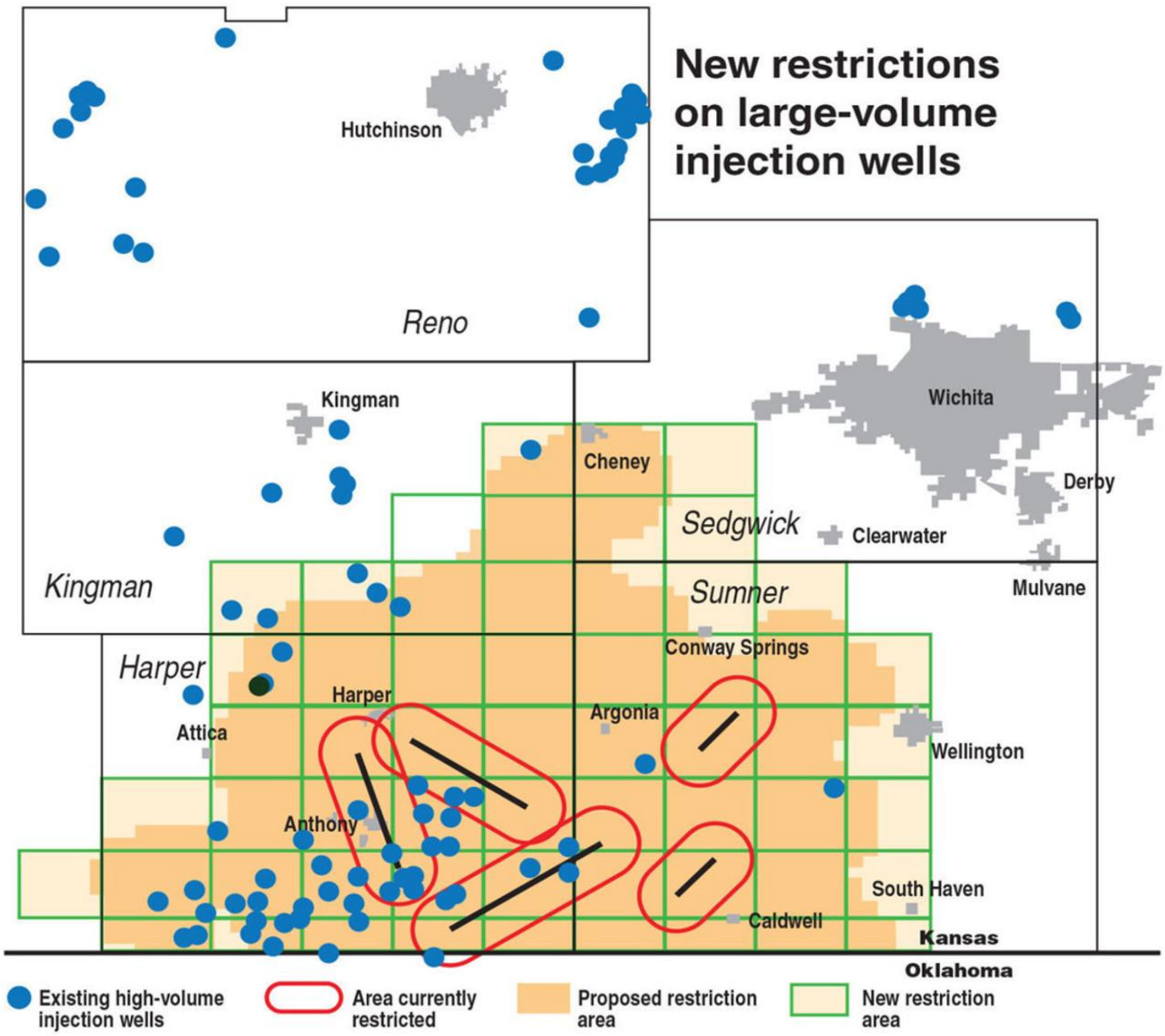

Figure 2: In March 2015, the Kansas Corporation Commission issued an order reducing the daily allowable limit from 30,000 to 8,000 barrels a day. Compliance had to be met within 100 days of the order issue date (Green, 2016).

Chapter 2 - General Settings

2.1. Kansas Geologic Setting

Kansas is located on a flat lying extension of the stable Archean Canadian Shield, the foundation rock of the North American continent (Merriam, 1963). The rocks that form the basement underlying Kansas were accreted during the Proterozoic (Merriam, 1963). Pre-Mississippian depositional structures are difficult to recognize because deformation and erosion after their original deposition commonly have altered their shape and configuration considerably (Merriam, 1963), (Figure 3). The sedimentary rocks that overlie the basement complex are thin-bedded units that are horizontal to sub-horizontal each other. Many of these rock units were deposited between the Cambrian and Pennsylvanian periods when a series of transgressive and regressive cycles deposited many of the carbonate units and marine shales (Merriam, 1963). Two prominent structural uplifts that affect the Paleozoic rocks in Kansas, the Nemaha uplift and Central Kansas uplift (CKU), (Figure 4), represent significant Early Pennsylvanian deformation events are likely associated with the Ouachita Orogeny when pre-Pennsylvanian rocks in the region were folded, faulted, uplifted, and severely eroded along the Ouachita Mountains orogenic belt in Arkansas (Newell et al., 1989; Dolton et al., 1989; Cardott and Chaplin, 1993). The Ouachita Orogeny began during the Early Pennsylvanian Period (~318 Ma) as the South American plate encroached upon the continent of Laurentia (Keller, 2012). The orogeny compressed strata on top of nearby platform rocks in a north and westward orientation. Since little tectonic activity has occurred in the region following this orogenic event, the resulting basement structure of Kansas resembles that of modern day Kansas due to stable plate tectonics within the mid-continent (Merriam, 1963), (Figure 4).

Sumner County lies within the Sedgwick basin and is bounded to the east by the Nemaha Uplift which separates the Cherokee basin from the Sedgwick basin (Figure 4). To the northwest of the Sedgwick Basin, is the Central Kansas Uplift which formed through a series of warping and truncations of the granitic basement rock in Precambrian times (Koester, 1935).

Structural maps of the Precambrian basement and isopach maps of the Arbuckle Group (Figure 4) illustrate both the Central Kansas Uplift and the Nemaha Ridge prior to Arbuckle deposition. Deformation that occurs during and after the Arbuckle deposition appears to be minor (Franseen et. al., 2004).

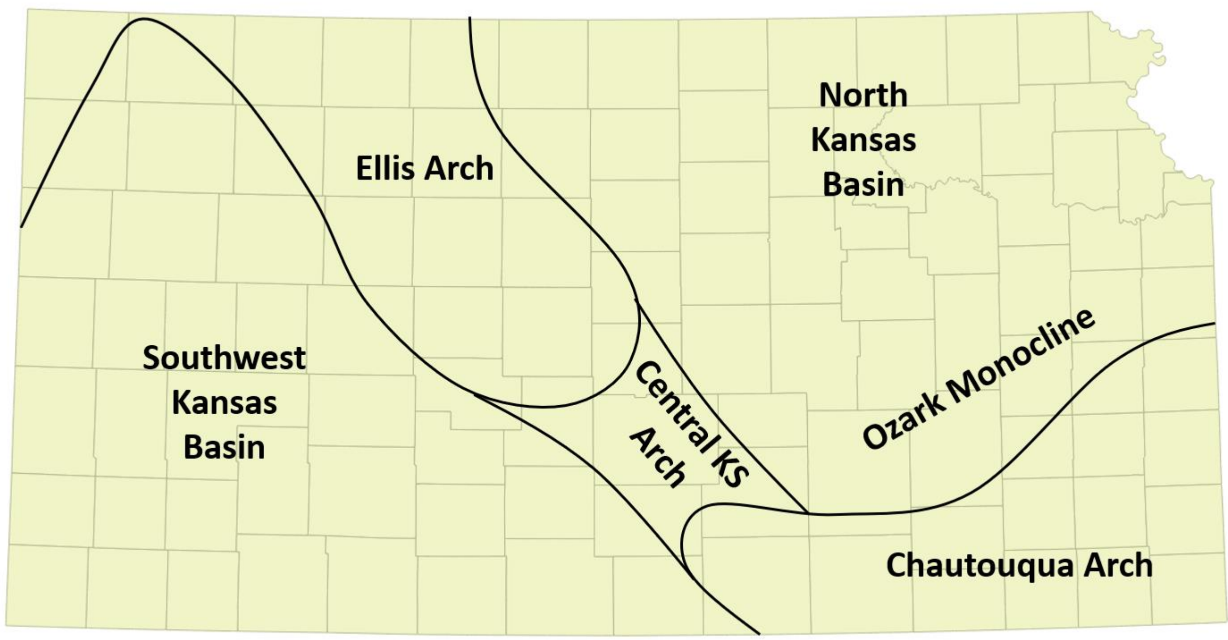

Figure 3: Pre-Mississippian post-Devonian Period Kansas. The structures represented (thick black lines) comprise the basement structure of Kansas prior to the Mississippian. The Ouachita Orogeny took place later folding and compressing the basement rocks to form the modern-day Proterozoic basement structure (Merriam, 1963).

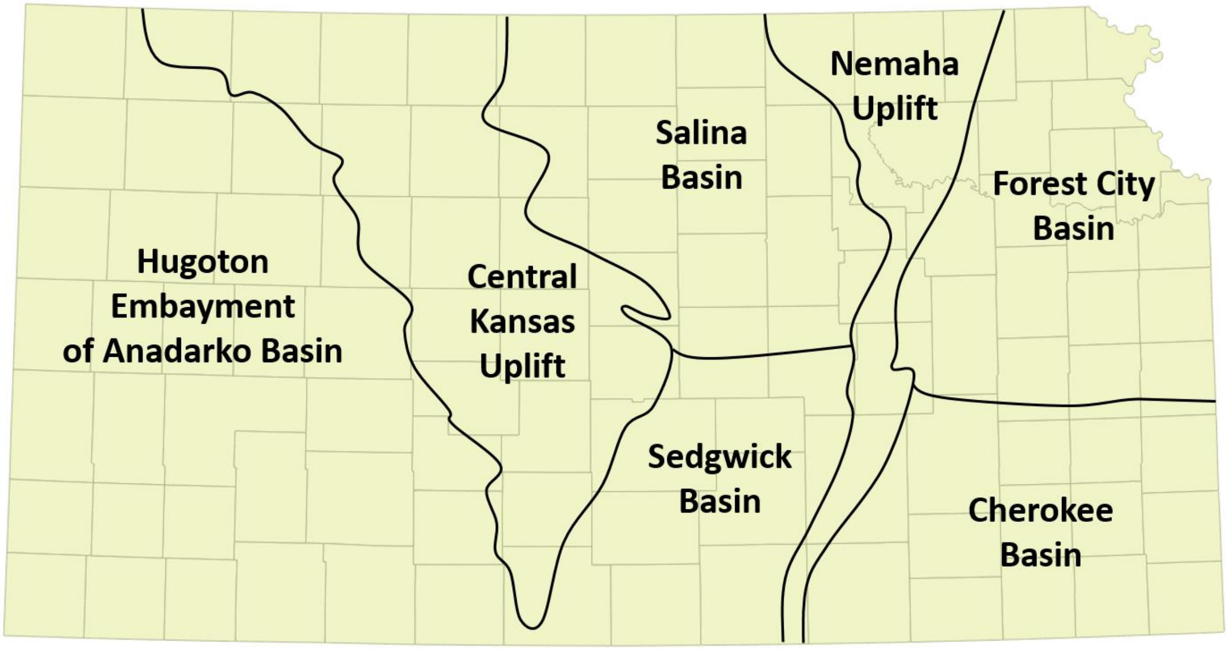

Figure 4: Early Pennsylvanian structure of Kansas. The boundaries (thick black lines) depict the general basement structures of Kansas in the early Pennsylvanian. Little tectonic activity occurred following the development of the of these structural uplifts and depressions and the basic structure of the Kansas Precambrian basement closely resembles this of modern day. (Merriam, 1963)

2.2. Oklahoma Geological Setting

Oklahoma has had a more complicated Proterozoic through the Pennsylvanian tectonic history than Kansas. Oklahoma's oldest rocks are Precambrian igneous and metamorphic rocks that formed about 1.4 billion years ago on which younger sedimentary rocks were deposited (Johnson, 2008). The principal mountain belts, the Ouachita, Arbuckle, and Wichita Mountains, are located in the southern part of Oklahoma (Johnson, 2008), (Figure 5). These mountain belts were the sites of folding, faulting, and uplifting during the Pennsylvanian Period (Johnson, 2008). In north central Oklahoma, basement rocks are located at approximately 1.7 km below sea level. To the south and southwest, the basement depth increases to 9.14 km - 12.19 km beneath deep sedimentary basins (Johnson, 2008), (Figure 6). Adjacent to the basins, basement rocks were uplifted above sea level in two major fault blocks exposed in the Wichita and Arbuckle Mountains (Figure 5), generating erosion and unconformities (Johnson, 2008). The fault block lineaments in Figure 6, closely resemble the ~N310˚ strikes of the fault planes present within south-central Kansas and north central Oklahoma (KGS: Open File Report 97-72, 1998), (Figure 7).

The Pennsylvanian Period was a time of major tectonic activity in Oklahoma: with mountain building and related subsidence of the Anadarko and Arkoma basins in the south; gentle raising and lowering of broad areas in the north. Uplifts in Colorado and New Mexico gave rise to the mountain chain referred to as the Ancestral Rockies (Johnson, 2008). Sediments deposited before the Wichita, Arbuckle, and Ouachita Uplifts were lithified, deformed, and uplifted to form major mountains, while nearby basins subsided rapidly and received these sediments eroded from the highlands (Johnson, 2008). During the Pennsylvanian this area was affected by five different orogenic pulses. Each orogenic pulse affected different areas by varying degrees of deformation (Johnson, 2008).

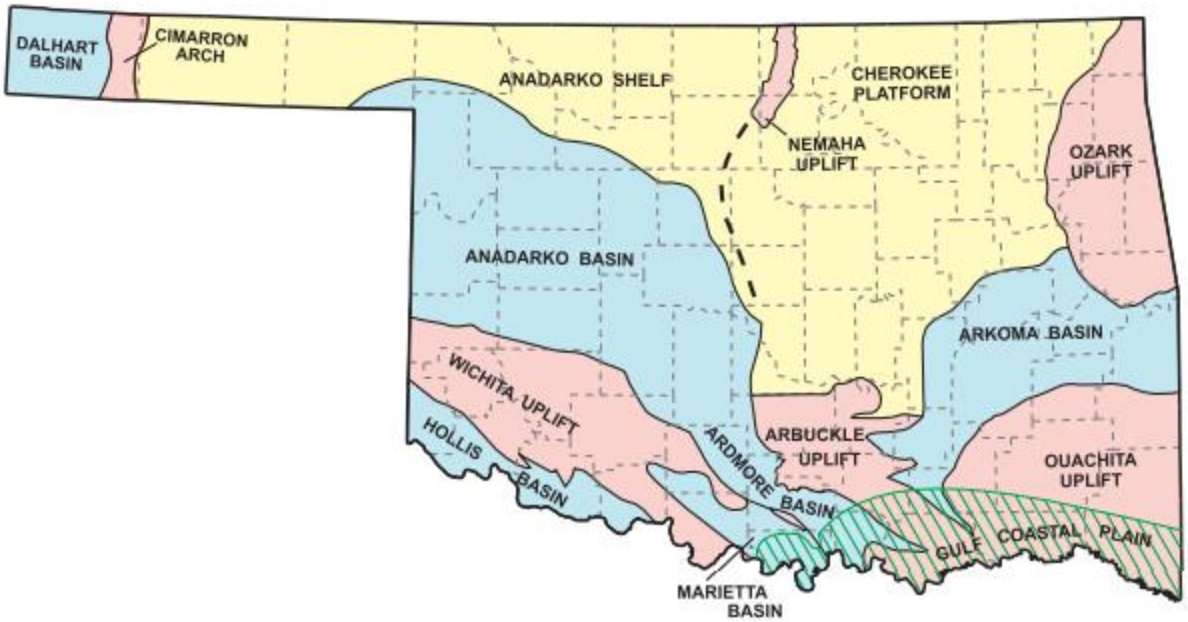

Figure 5: Major geologic provinces of Oklahoma (Johnson, 2008).

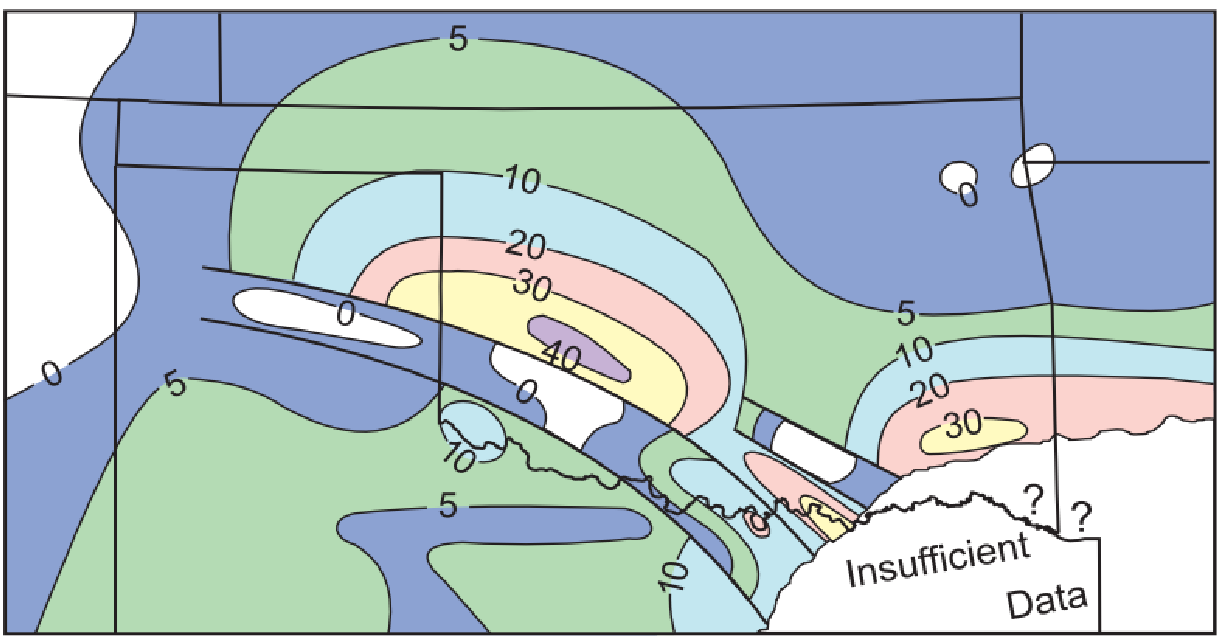

Figure 6: Generalized contours showing elevation (in thousands of feet below sea level) of the eroded top of Precambrian and Cambrian basement rocks in Oklahoma and parts of adjacent states (Johnson, 2008).

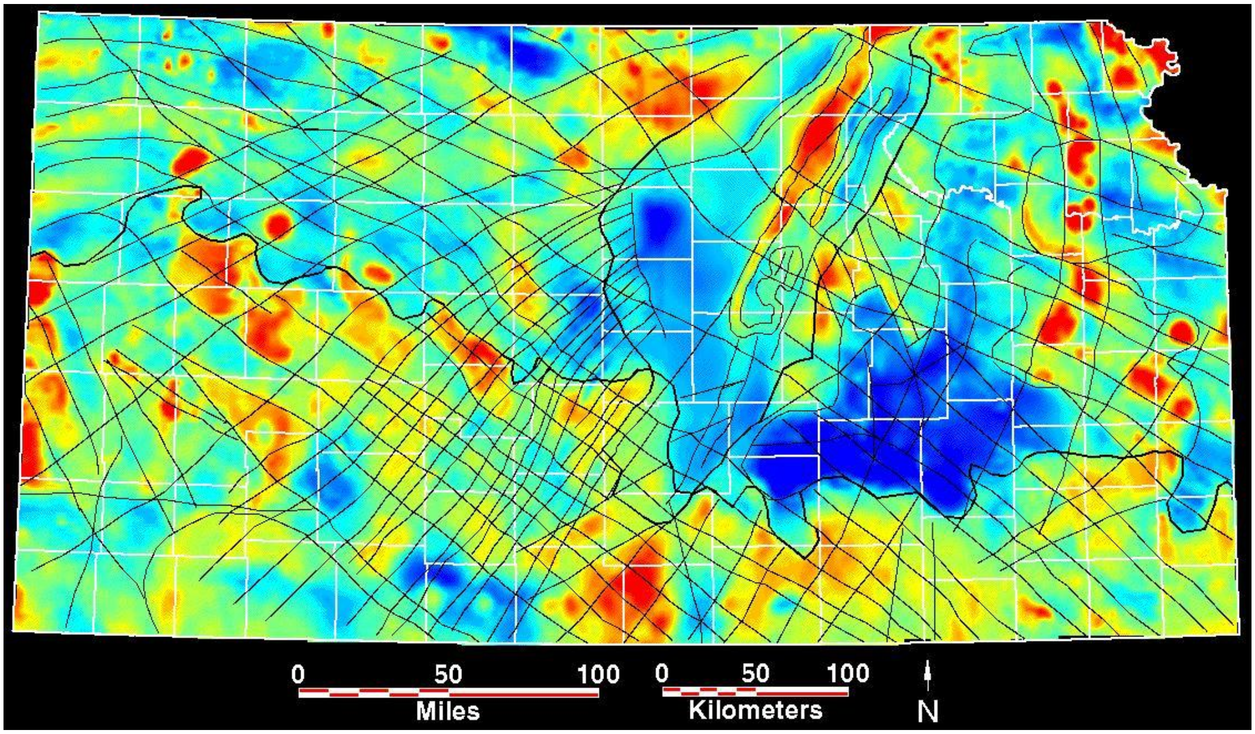

Figure 7: Regional magnetics map displaying the similar lineament orientations (~N310˚) present in Kansas (KGS: Open File Report 97-72, 1998).

2.3. Seismic Study Area

The study area covers the Anson-Bates and Wellington oil field, located within Sumner County, Kansas (Merriam, 1963; Ohl and Raef, 2014), (Figure 8). The expanse of the oil fields is approximately 47 km^2 in the north-central area of Sumner County. The Wellington and Anson-Bates were first discovered in the late 1920's, with peak production occurring in the late 1960's. The study area consists of a large, heterogenous dolomitic sequence that is approximately 300 m thick known as the Arbuckle Group that occurs from 1.3 km to 1.6 km depth. The Arbuckle Group has been assessed and is utilized as a large-scale saltwater disposal reservoir because it is thick, porous, and it is bounded above by numerous impermeable shale layers that negate the upward flow of wastewater into the potable water table. The stratigraphy of the study area is illustrated in Figure 9 (Carr-et al, 2005) with the focal periods consisting of the Mississippian, Ordovician, and Cambrian including the dolomitic Arbuckle and Mississippian limestone groups.

KGS 1-32 well is a monitoring well managed by the Kansas Geological Survey located within Wellington Field. The well has a large suite of geophysical well logs available through the interactive oil and gas website operated and updated by the Kansas Geological Survey. The dense suite of geophysical logs helps to define the underlying stratigraphic sequences and their individual characteristics (Figures 10 and 11).

Most faults related to the Nemaha Ridge are orientated N30˚E. The active strike-slip Humboldt fault zone bounds the Nemaha Ridge to the east (Figure 8). The Nemaha Ridge is located in the eastern portion of Sumner County. The largest earthquake in Kansas history originated from the Humboldt Fault and registered an estimated magnitude of 5.1 in 1867 (KGS: Kansas Earthquakes, 2018).

The Nemaha fault (Merriam, 1963), (Figures 8 and 12) is a high-angle, reverse fault that is generally down-to-the-east in northern Kansas with an estimated vertical displacement of 760 m (McBee, 2003). The Nemaha Fault zone is regarded as a narrow transpressional fault zone that in Oklahoma experienced initial movement at least as early as Middle Ordovician (McBee, 2003). The geometry of the system and the fact that the Nemaha appears to have movements affecting sedimentation and erosion during the lower Paleozoic strongly suggest that the Nemaha had its origin in the same tectonic regime as the original Midcontinent Rift System (1200 Ma) (Gerhard, 2004). Basically, it is a wrench-fault zone of limited horizontal displacement, where fault separation along the trace changes in several places from high-angle normal to high-angle reverse, and where it is associated with pull-apart grabens and/or horst (pop-up) structures (McBee, 2003). Near the Oklahoma border, vertical displacement decreases and reverses to down-to-the-west (Aber, 2008). The general orientation of the Nemaha Ridge in north-central Oklahoma and south-central Kansas is N-NE (Figure 8).

Regional stress field orientations from this research study support the findings of Alt and Zoback (2017), which identifies the maximum horizontal stress, SH_{max}, acting on the study area at approximately N074˚ with the minimum horizontal stress, SH_{min}, oriented roughly N164˚.

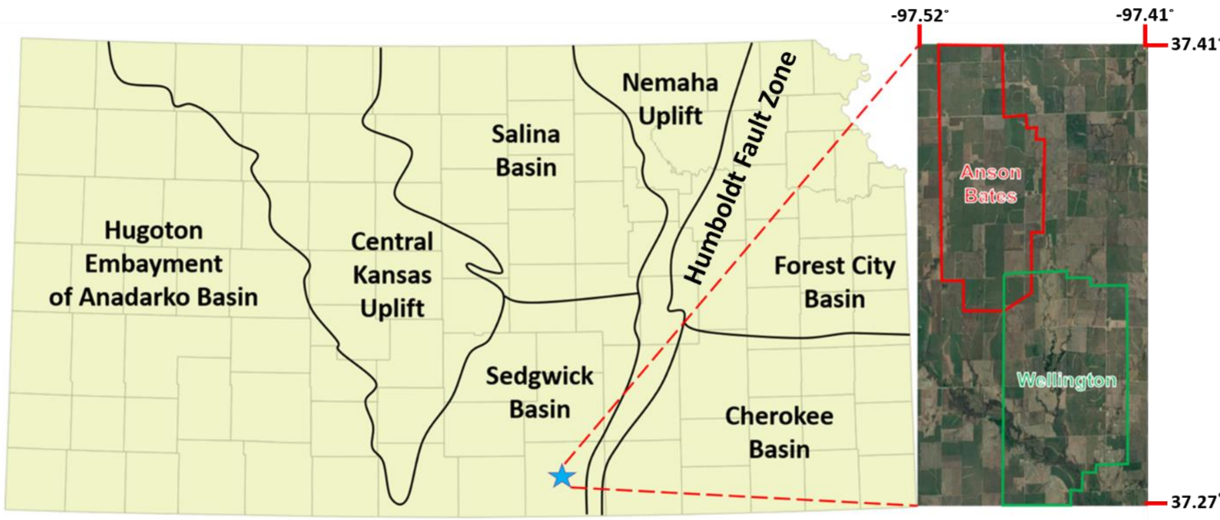

Figure 8: Location of Anson-Bates and Wellington Fields seismic survey study area indicated by the blue star. The basins and uplifts outlined above in black illustrate the Early Pennsylvanian structural framework of the underlying Proterozoic basement (Merriam, 1963, Ohl and Raef, 2014).

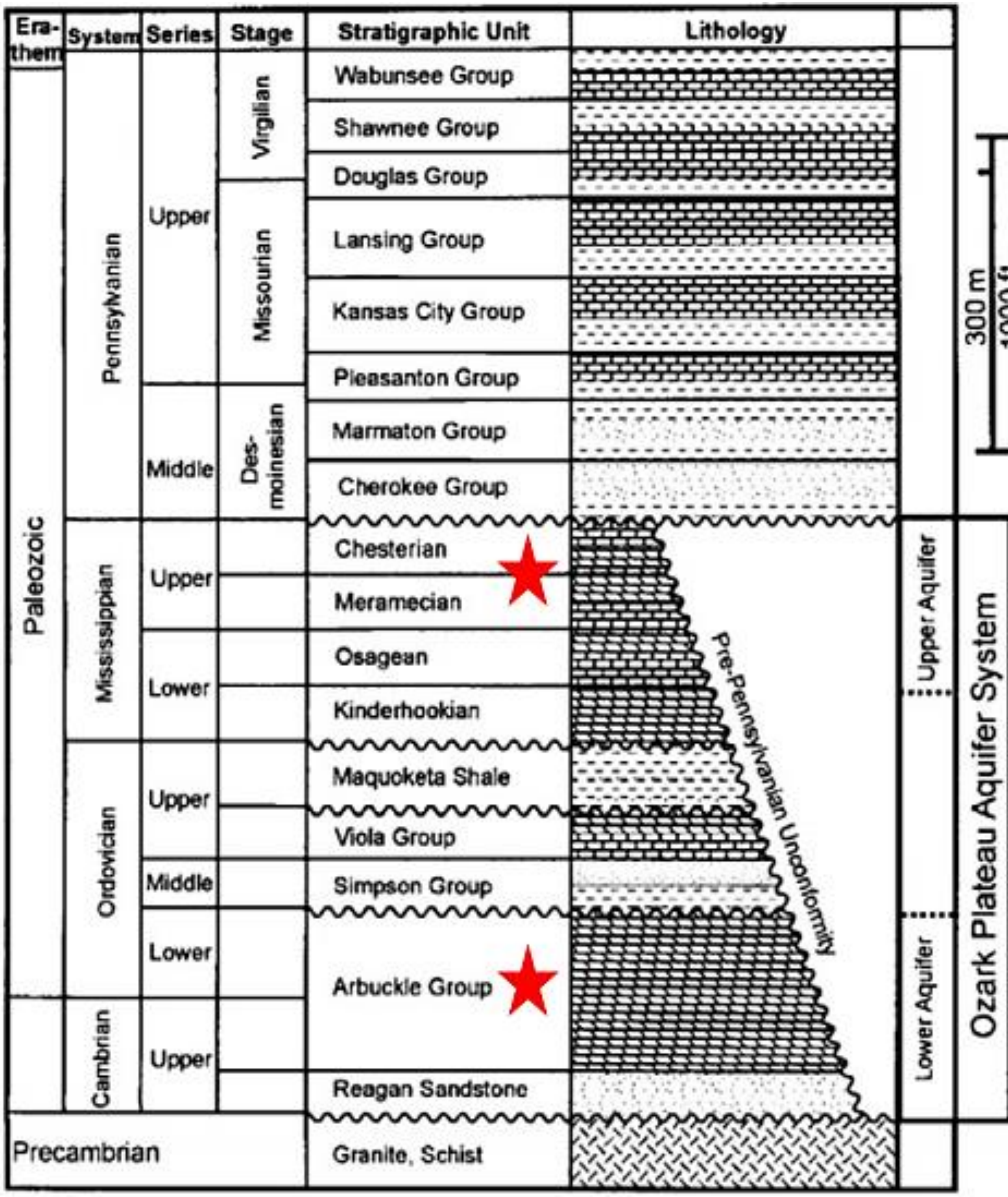

Figure 9: Generalized stratigraphic column of the subsurface geology beneath the seismic study area of south central Kansas in Sumner County. Disposal zones marked by red stars (Carr-et al, 2005).

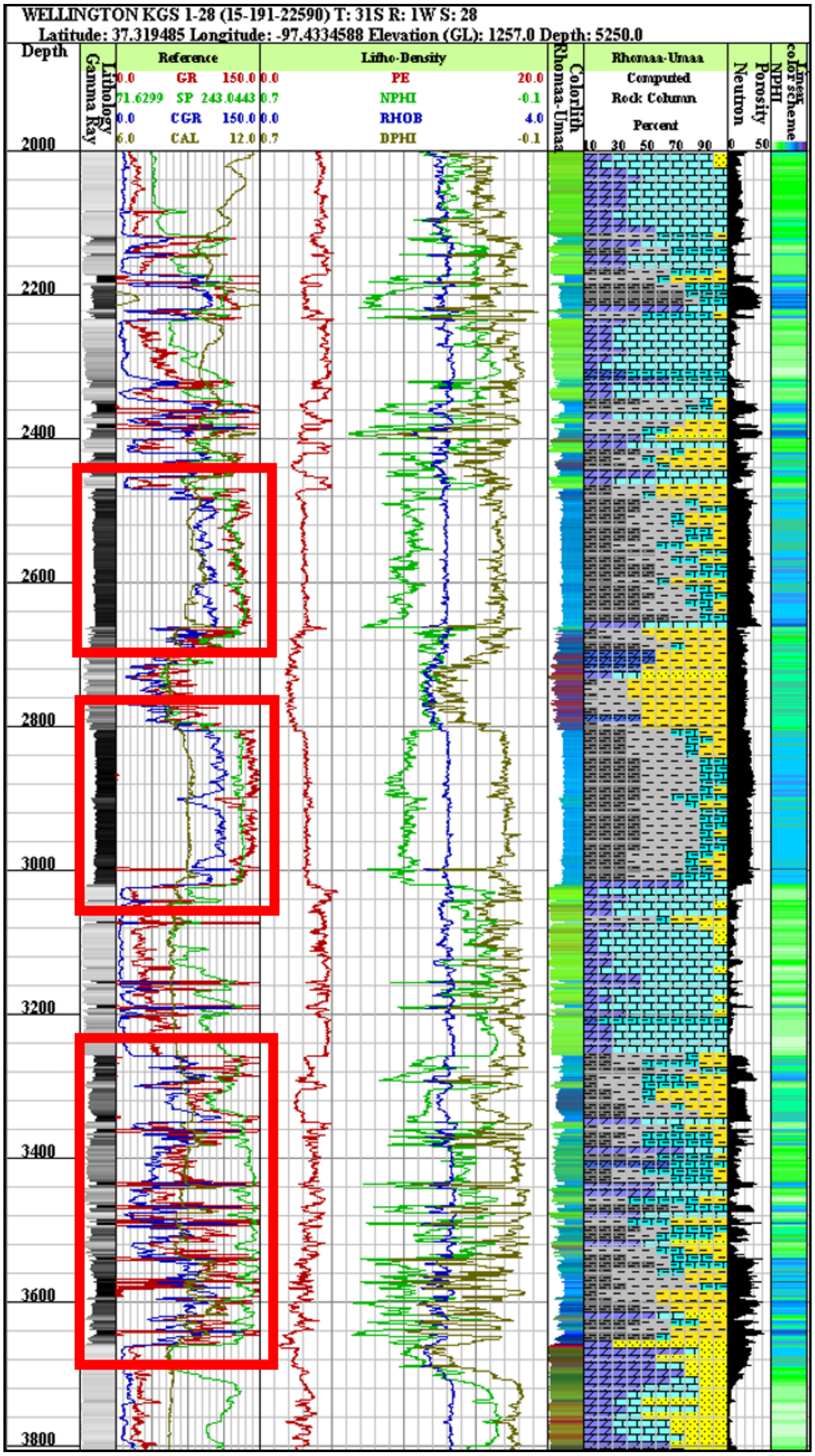

Figure 10: KGS 1-32 geophysical well log (2000-3800 feet) (GR-gamma ray, SP-spontaneous potential, CAL-Caliper, PE-photoelectric, NPHI- neutron porosity, RHOB-density, DPHI-density porosity) illustrating several impermeable sealing shale layers outlined by the red boxes (Ohl and Raef, 2014).

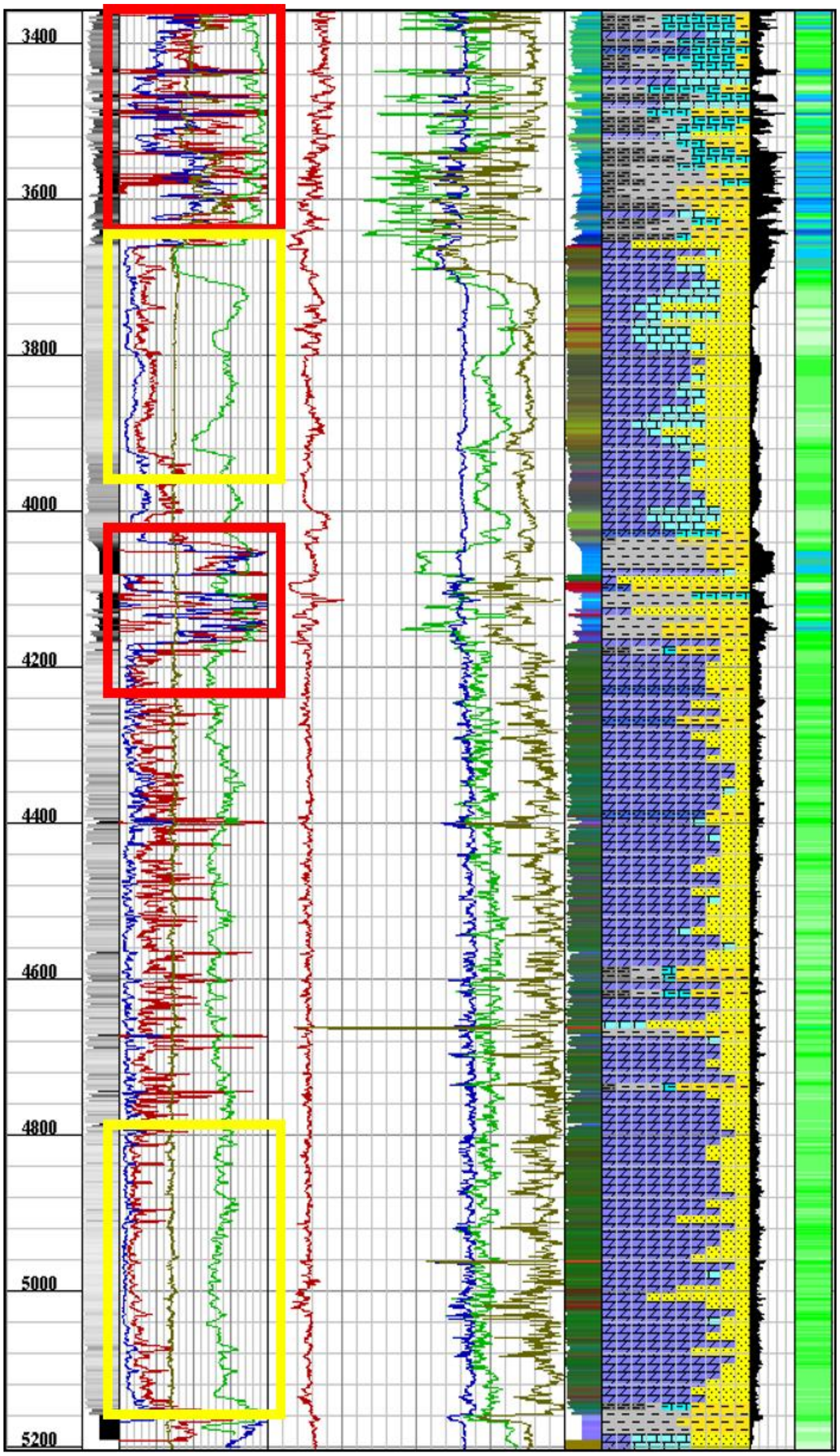

Figure 11: KGS 1-32 geophysical well log (3200-5200 feet) illustrating the sealing formations (red boxes) and the carbonate disposal zones (yellow boxes) present within Anson-Bates and Wellington Fields (Ohl and Raef, 2014).

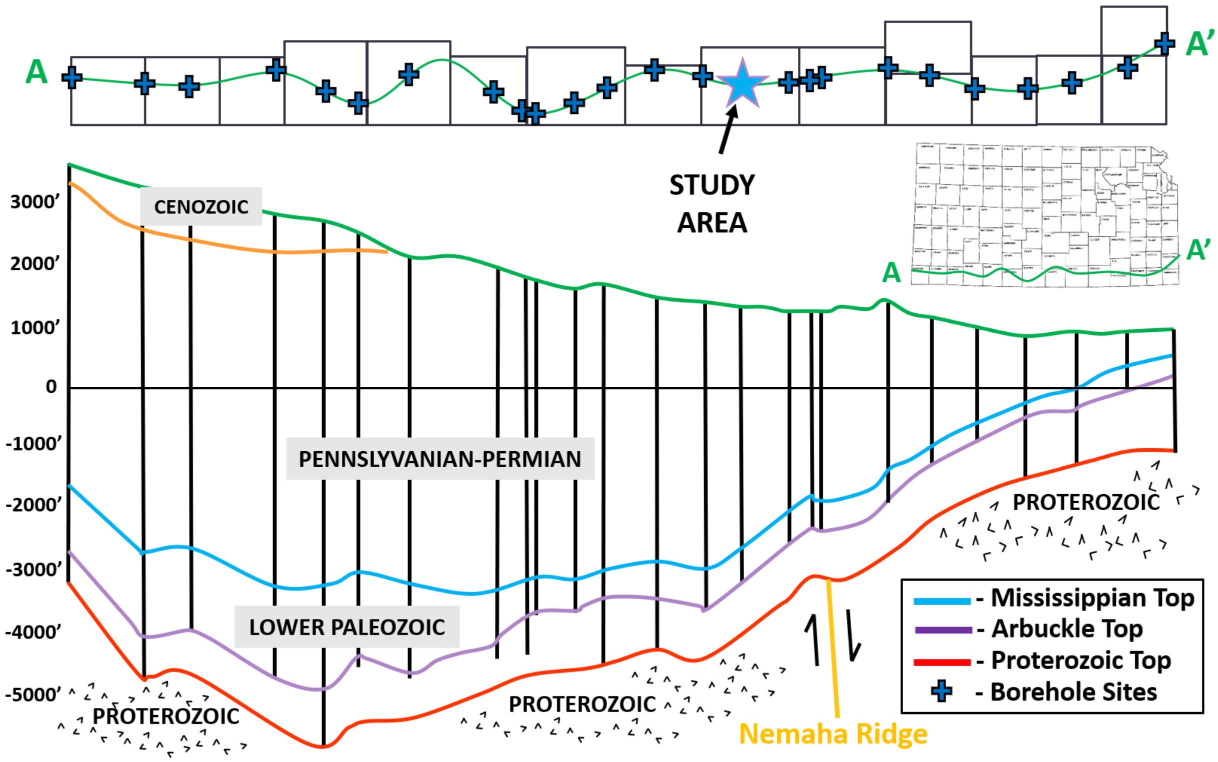

Figure 12: Cross-section of southern Kansas counties that share a border with the Oklahoma counties located within the regional focus area. Nemaha fault plane (gold line) separates the opposing hanging wall and foot wall. Fault block direction indicated by the black arrows. The Nemaha Ridge extends from southern Nebraska to central Oklahoma with an orientation of N030˚ degrees approximately. The blue star depicts the location of Anson-Bates and Wellington Fields (Modified from Merriam, 1963).

Chapter 3 - Seismic Data

3.1. Earthquake Waveform Data

The earthquake data used for this research was collected by United States Geological Survey (https://earthquake.usgs.gov) and the Kansas Geological Survey (http://www.kgs.ku.edu/Geophysics/Earthquakes/index.html). The KGS has a network of 13 seismograph stations positioned throughout the state, six of which are located within the south-central Kansas study area (KGS: Kansas Earthquakes, USGS: Induced Seismicity, 2018), (Figure 13). The USGS has a high-density network of 14 seismograph stations within Harper and Sumner County. The USGS seismograph network is a part of the ongoing USGS Induced Seismicity Project. The aim of which is to collaborate with geoscientist from the Kansas and Oklahoma Geological surveys, the KCC, and the Kansas Department of Health and Environment to better understand the cause and effect of the increased seismicity within the region (Buchanan, 2015).

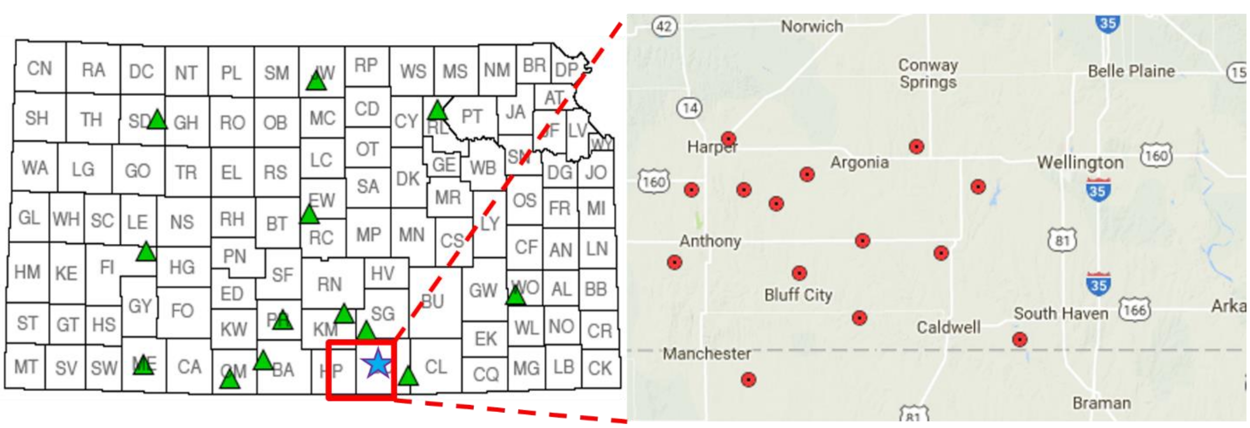

Figure 13: Widespread KGS seismograph stations located within Kansas on the left (green triangles). Dense seismograph network operated by the USGS Induced Seismicity Project on the right (red dots) (KGS: Kansas Earthquakes, USGS: Induced Seismicity, 2018).

Waveform data from earthquakes registering magnitude 3.3 or larger were processed by USGS researchers who rendered focal mechanisms representative of fault orientation and type. The result is 99 well-constrained earthquake focal mechanisms located within the study region, broken down into 32 normal and 67 strike-slip events (USGS: Earthquake Database, 2018). The focal mechanisms have two possible nodal planes and the proper orientation of the fault must be determined.

An example of two possible slip planes and their differing orientations is represented by Figure 14 (Rowan, 2013). Determining the regional stress tensor, allows the interpreter to more accurately select the proper slip plane for those cases where observing fault plane movement is not possible due to depth of burial. The orientations of the strike-slip focal mechanisms in Figure 14 (Rowan, 2013) closely match the orientations of those within this research study. The Nemaha Ridge is oriented approximately N030˚ (USGS: Earthquake Database, 2018, Figure 8). Many of the focal mechanisms within the study area striking N030˚-N060˚ exhibit right lateral movement along the nodal plane (Figure 15) determined by the regional stress tensor and their slip tendency.

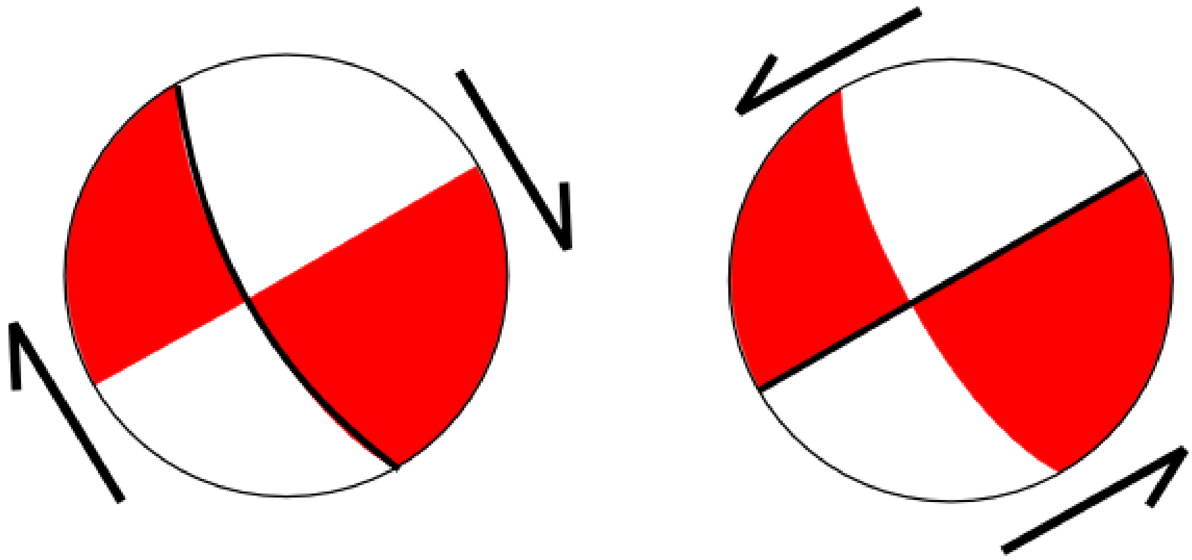

Figure 14: Two possible fault plane orientations regarding a strike slip focal mechanism. Black lines on each focal mechanism indicate the possible slip plane and the associated arrows with each image illustrate the direction of movement. The image on the left illustrates dextral slip on NW-SE trending fault plane. The focal mechanism on the right depicts sinistral movement on NE-SW trending fault plane (Rowan, 2013).

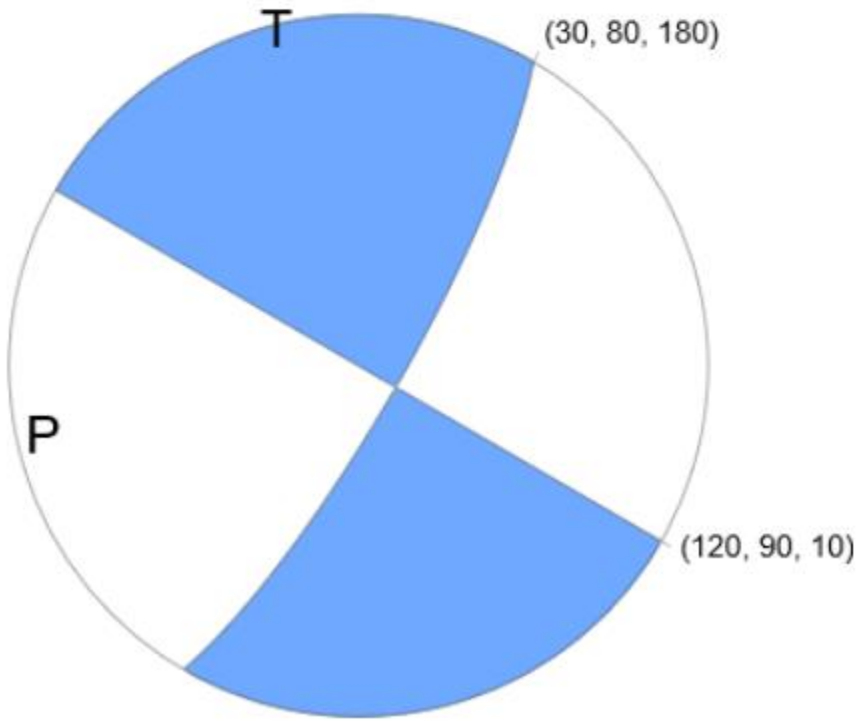

Figure 15: Focal mechanism associated with the orientation of the Nemaha Ridge. The slip plane was determined to strike N30˚E degrees and dip 80˚ using the regional stress state and slip tendency modeling. The fault plane strikes NE-SW and exhibits a right-lateral strike slip movement (USGS: Earthquake Database, 2018)

3.2. 3D P-wave Seismic Survey Data

The Wellington Field and Anson Bates Field 3D seismic survey dataset was obtained from an earlier Department of Energy-sponsored study (Ohl and Raef, 2014). The focus of the 3D survey was to image the Mississippian and Cambro-Ordovician reservoirs to assess their potential as disposal zones and to determine a suitable site for a carbon dioxide sequestering well. The survey was performed in the Anson-Bates and Wellington Fields which covers approximately 47 km^2. The purpose of the 3D seismic data for this project was to utilize spectral analysis tools to enhance imaging of faults affecting the Proterozoic basement. Sedimentary faults are present and easily identifiable in the upper Mississippian carbonate zone within Anson-

Bates Field (Figure 29). As the depth of investigation increases, the seismic resolution decreases due to loss of seismic energy, known as attenuation: There are two types of attenuation: anelastic (absorption) and elastic (scattering) (Reynolds, 2011). Absorption, reflection, and refraction of seismic waves at differing lithological boundaries accounts for the loss in energy at increasing depths. Attenuation is frequency-dependent and linked to dispersion, which is the frequency dependence of velocity (Reynolds, 2011). Seismic wavelength is calculated by:

$$\lambda = \nu / f \quad (1)$$

Where λ is the wavelength in meters, ν is the velocity in meters per second, and f is the frequency in hertz. Vertical seismic resolution is calculated by, and defines, the seismic bandwidth that can't be used to delineate different stratigraphic layers (Widess, 1973; Reynolds, 2011). Broader bandwidths mean better resolution for a given depth of investigation, in general, but seismic resolution deteriorates with increasing depth. In this study, spectral whitening has been applied to the data to increase the usable bandwidth and therefore, the resolution at (and below) the basement surface.

Chapter 4 - Computing Pore Fluid Pressure Required for Fault Reactivation

4.1. Regional Stress Tensor Determination

The first step in determining the pore fluid pressure required for reactivation was determining the orientation of the regional stress field present within the underlying Proterozoic basement and identifying the proper stress shape ratio, $\Phi = \frac{\sigma 2 - \sigma 3}{\sigma 1 - \sigma 3}$, (Angelier,1984; Delvaux, 2016), of south-central Kansas and north-central Oklahoma. Nodal plane data from 26 earthquakes with magnitudes 3.9 or greater were utilized to determine the regional stress state, as the larger magnitude seismic events are a better representation of the active regional stresses (Leclere and Fabbri, 2013). The nodal plane data required for calculating the regional stress tensor included identifying the dip direction, dip angle, and rake of one of the two possible earthquake nodal planes.

We used Win-Tensor (http://www.damiendelvaux.be/Tensor/WinTensor/win-tensor.html) paleostress reconstruction software for tectonic stress determination from earthquake focal mechanism data. Win-Tensor allows us to reconstruct the four parameters of the reduced paleostress - or stress-tensor - (orientation of the three principal stress axes and the stress shape ratio) (Delvaux, 2016). The Win-Tensor program uses function (F5; also called F3 in Delvaux and Sperner, 2003) that minimizes both the misfit angle α between the actual slip vector and the theoretical slip vector, and the shear stress/normal stress ratio (τ/σ_n) acting on the fault plane (Leclere and Fabbri, 2013). A nodal plane that results in a small misfit angle α indicates that the regional stress field dictates the movement along the slip plane. A large misfit angle α indicates that slip is not governed by the regional stress field but more likely controlled by local stress perturbations. The magnitudes of the shear stress τ and the normal stress σ_n provide an indication about the slip tendency of the fault planes (Leclere and Fabbri, 2013). The slip tendency, T_S, of a fault plane is the fault's potential for reactivation based on the orientation of the principal stresses and the ratio of shear stress, τ, to normal stress, σ_n, acting on that surface. Faults with large shear stresses coupled with low normal stresses are more easily reactivated than those with large normal stresses and a small shear stresses. Values for the F5 function vary from 0 to infinity. If the F5 value is small, then the fault plane is dictated by the regional stress tensor and its tendency for fault slip is favorable (Leclere and Fabbri, 2013).

A misfit angle filter of 30˚ or less was applied to the dataset to determine the appropriate orientation of the nodal plane where fault slip was more likely to occur. The nodal planes that fulfilled the misfit angle criteria were optimized and used to determine the regional stress tensor and the stress shape ratio. The derived regional stress tensor determined that the maximum principal stress, σ_1, azimuth is N075˚ with a plunge of 88˚; the intermediate principal stress, σ_2, azimuth is N254˚ with a plunge of 2˚; the least principal stress, σ_3, is oriented N344˚ and plunging 1˚. The maximum horizontal stress SH_{max} orientation is N074˚ and the minimum horizontal stress SH_{min} azimuth is N164˚, which aligns perfectly with the orientation of the minimum principal stress σ_3 stated above. The resulting stress shape ratio, ϕ, from the regional stress tensor calculations yielded a value of 0.73. It is important to note here that the three main fault types have differing principal stress orientations and the stress shape ratio, ϕ, ascertained was generated using nodal plane data from 14 strike-slip faults and 12 normal faults. The resulting regional stress tensor agrees with the well-defined results of the World Stress Map (2016), previous regional research (Alt and Zoback, 2014; Schwab, 2016), and achieved the highest World Stress Map data quality ranking of an ‘A’ for excellence, and with results from regional studies (e.g., Schwab et al., 2017; Jenning and Bidgoli, 2016; Nolte et al., 2017).

4.2. Fault Mechanics

Fault planes can be identified as favorably oriented, unfavorably oriented, or severely misoriented (Sibson, 1990) based on the type of faulting (i.e. reverse, strike-slip, or normal) and, fault plane orientation (i.e. dip/strike) in relation to the effective stress field. The Mohr stress diagram is a 2-dimensional representation of a stress tensor acting on an plane represented graphically by an X-Y coordinate plane. Basic components of every Mohr circle include the absolute values of the maximum compressive stress, σ_1, the intermediate stress, σ_2, and the least compressive stress, σ_3, which comprise the elements of the X-axis. The Y-axis is the sum of shear stresses acting within the fault plane and therefore perpendicular to the normal stresses (Burg, 2015). The Mohr-Coulomb failure envelope was developed following a series of laboratory experiments designed to identify how various rocks react to triaxial stresses at differing confining pressures. Shear and principal stresses that plot below the failure criterion are considered stable. Stresses that plot on or above the failure envelope are considered unstable and will result in brittle shear failure. When any portion of the Mohr stress circle contacts the Mohr-Coulomb envelop with $\sigma_3 > 0$ shear failure occurs, if $\sigma_3 < 0$ tensile or hybrid failure occurs (Burg, 2015). Generally, an increase in shear stress to some critical value in response to increasing strain due to movement of opposing fault blocks is the leading development of seismic events. The effective stress burden on a rock body is the total stress minus the pore fluid pressure. When pore fluid pressures are added to the equation, the shear stress required for fault plane reactivation is reduced, resulting in a shift of the stress circle to lower shear regimes (Burg, 2015), (Figure 16).

The largest change in reservoir pressures within Kansas occurs near the highest rate injection wells, with most of the change occurring in the past five years (Bidgoli et al., 2016; Schwab et al., 2017). Increasing the pore fluid pressure within a region greatly reduces the amount of effective stress required to initiate fault plane activation (Figure 16). These may be in the form of fault reactivation of non-cohesive faults or fracture propagation of a cohesive fault plane (Sibson, 1990).

The slip-tendency, $Ts = \frac{\tau}{\sigma n}$, of a fault plane can be calculated from its orientation relative to the field stress, fault type, nodal stress field, normal stresses, static coefficient of rock friction, and effective pore fluid pressures at fault depth. The stability of existing faults within a seismogenic zone is likely to be governed by an empirical failure criterion of Coulomb form:

$$\tau = C + \mu_s \sigma_n' = C + \mu_s(\sigma_n - P_f) \quad (2)$$

where C is the cohesive or cementation strength (which for an existing fault may be rather low), μ_s, is the static coefficient of rock friction, P_f is the fluid pressure within the rock mass, and τ and σ_n are, respectively, the resolved shear stress and normal stress components on the fault (Sibson, 1990). For a fault inclined to the orientation of σ_1 at an angle θ_r, we have relationships:

$$\sigma_n = \frac{\sigma_1+\sigma_3}{2} - \frac{\sigma_1-\sigma_3}{2}\cos 2\theta_r \quad (3)$$

and

$$\tau = \frac{\sigma_1-\sigma_3}{2}\sin 2\theta_r \quad (4)$$

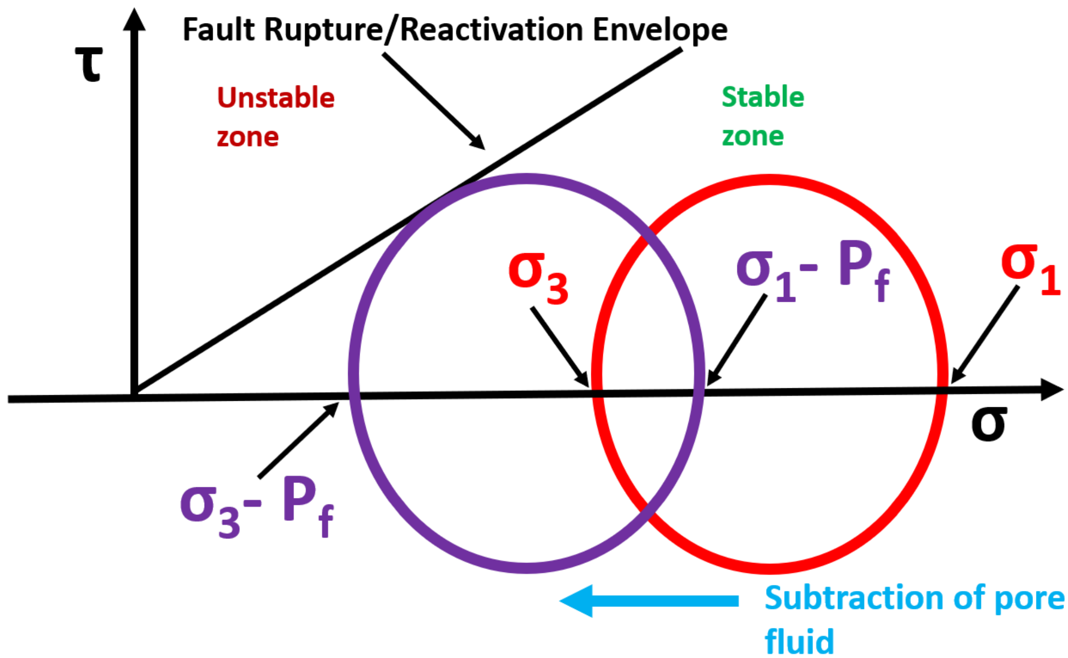

Figure 16: Mohr-Coulomb criterion for cohesionless fault planes illustrating the effect of pore fluid pressure increases on a Mohr circle representing the minimum and maximum stresses acting on a fault plane. An increase in pore fluid pressure, decreases the shear stress required for fault reactivation to occur.

4.3. Calculating Q-Values

Based on regional stress tensor parameters fault reactivation potential, Q, was computed using methods from Leclere and Fabbri (2013). Effective stress ratios, $Q = \frac{\sigma_3'}{\sigma_1'}$, were determined utilizing regional stresses to better understand fault orientations and their susceptibility to reactivation due to pore fluid pressure increases. In addition, the orientations of both the normal and strike-slip fault populations could be judged contemporaneously if both are associated to the formation of a trantensional basin during the five orogenic events of the Pennsylvanian Period.

Sibson (1985) introduced three classes of fault orientation and the ratio of effective principal stresses to induce sliding:

$$R_{optimal} = \frac{\sigma_1'}{\sigma_3'} = \frac{1+u_s \cot\theta_r}{1+u_s \tan\theta_r} \quad (5)$$

where θ_r is the angle of reactivation. “Favorably oriented” faults have R values between the minimum R-value ($R_{optimal}$) and ($R_{optimal}$ x 1.5), “Unfavorably oriented” faults have R values larger than 1.5 x $R_{optimal}$, and "Severely misoriented” faults have negative R values (Sibson, 1985; Leclere and Fabbri, 2013) The effective stress ratio, Q, introduced by Leclere and Fabbri (2013) is the inverse of Sibson’s R-values where, $Q = \frac{\sigma_3'}{\sigma_1'}$. The Q value stereo plots demonstrate that the strike-slip fault is favorably oriented, and the normal fault is severely misoriented. Their poles indicate the Q value of the reactivated fault plane (Figures 17 and 18). The input information required to generate the plots includes: a regional stress tensor, slip plane orientation, regional stress shape ratio, and the coefficient of static friction for granite. Where the pole of the slip plane plots on the stereoplot determines the Q-value assigned to that fault plane. On the generated stereoplots below (Figures 17 and 18), the blue region is associated with severely misoriented faults, the red region indicates favorably oriented faults, and the orange region indicates unfavorably oriented fault planes.

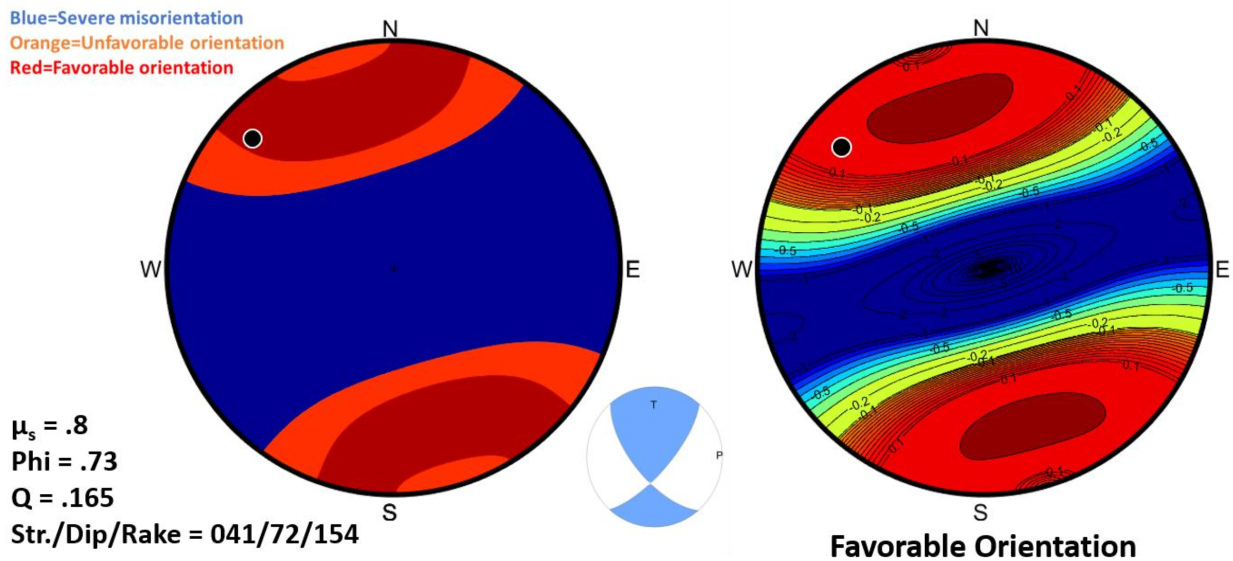

Figure 17: Contoured Q-value stereoplot of a strike-slip faulting event within the study region. The pole of the fault plane is used to determine its potential for reactivation. This event is favorably oriented at a static coefficient of 0.8. Its estimated theoretical pore fluid pressure required for reactivation is 38 MPa. At 0.6 μ_s its theoretical value is 14 MPa**.**

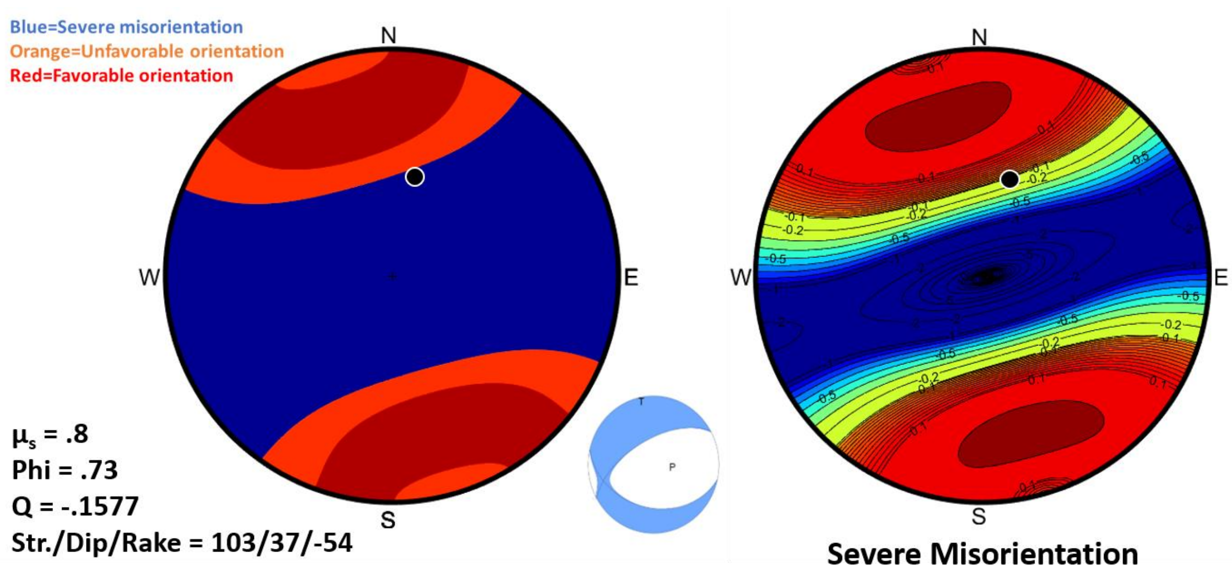

Figure 18: Contoured Q-value stereo plot of a normal faulting event within the study region. The pole of the fault plane is used to determine its potential for reactivation. This event is severely misoriented at static coefficients of 0.8. Its estimated theoretical pore fluid pressure required for reactivation is 45 MPa. At 0.6 μ_s its theoretical value is 34 MPa. This seismic event is not favorably oriented until 0.4 μ_s when its theoretical effective pore fluid pressure is 5 MPa.

4.4. Computing Effective Pore Fluid Pressure

Effective pore fluid pressures were determined using the maximum, σ_1, and minimum, σ_3, principal stresses, Q-values, and hydrostatic and lithostatic pressures present in the subsurface. As pore pressure increases with depth, it trends away from a hydrostatic gradient of 9.8 MPa/km and increases drastically to lithostatic gradient values of 16-24 MPa/km depending on bulk rock density and depth of burial (Bethke,1986), (Figure 20). Well logs from the KGS 1-32 indicate that the density of the granitic basement is approximately 2.75 g/cm^3 at a depth of 1.6 km. This equates to a maximum lithostatic gradient of approximately 24 MPa/km at 5 km depth.

To calculate the normal stresses acting on the fault plane, maximum and minimum principal stresses for normal and strike-slip faults had to be determined. The overburden stress of normal faults is the maximum principal stress, σ_1, acting on the fault plane and was calculated using rock densities from the KGS 1-32 well log. The overburden stress used to calculate the normal stress was determined using a basement density of 2.75 g/cm^3 for depths beyond 1.6 km and 2.55 g/cm^3 below 1.6 km for the sedimentary cover. The minimum principal stress, σ_3, acting on the normal fault was assumed to be 15.4 MPa/km from Figure 31. The principal stresses applied to strike-slip faults were intermediate values derived from Figure 31 in Appendix A (Schwab et al., 2017). The maximum principal stress, σ_1, for strike-slip faults was assumed to be 34.5 MPa/km and 17.6 MPa/km for the minimum principal stress, σ_3, utilizing the intermediate stresses associated with the strike-slip faults according the stress polygon (Schwab et al., 2017) in Appendix A. The normal stress acting on a fault plane can be calculated using:

$$\sigma_n = \frac{\sigma_1+\sigma_3}{2} - \frac{\sigma_1-\sigma_3}{2} \cos 2\theta \quad (6)$$

where θ is the angle between the normal stress acting on the plane of fracture and σ_1 (Burg, 2015).

The effective stress ratio, Q, can be rewritten to determine the pore fluid pressure required for reactivation by substituting $\sigma_1 - Pf = \sigma_1'$ and $\sigma_3 - Pf = \sigma_3'$ into the equation so pore fluid pressure is equal to:

$$Pore\ fluid, Pf = \frac{\sigma_3 - \sigma_1 Q}{(1-Q)} \quad (7)$$

(Leclere and Fabbri, 2013).

The pore fluid determined from this equation is the total pore fluid pressure required to reactivate the fault plane. Therefore, the pressure values based on hydrostatic gradient and lithostatic gradients were subtracted from the total pore fluid pressure to determine the added effective pore fluid pressure required aside from the existing fluid pressures from the fault's depth of burial. This eliminates the pore pressures associated with depth of burial and renders the theoretical additional pressures required to reactivate the fault plane. A hydrostatic gradient of 9.8 MPa/km was applied to the pore fluid data until a depth of 3.5 km was reached (Bethke,1986, Schwab et al., 2017). Beyond this depth, a lithostatic gradient of 19 MPa/km was applied. The pore fluid pressures beyond this depth cannot achieve the maximum lithostatic gradient values as the rock volume would be unable to contain the over-pressurized pore fluids (Bethke, 1986).

Chapter 5 - Results

5.1. Active Fault System in Proterozoic Basement

Faults within the basement complex follow two prominent orientation trends of ~N030˚ and ~N300˚ (Figures 19 and 20). Normal and strike-slip faults dominant the region with far fewer instances of reverse faulting occurring. These two faulting types are consistent with crustal extension and suggest the reactivation of a previously formed transtensional basin within the basement complex. Most fault orientations correspond to two dominant structural features present within the basement, the Nemaha Ridge and the Central Kansas Uplift. Earthquake epicenters were plotted, and fault lineaments were deduced from the propagation orientations of the earthquake epicenters (Figures 19 and 20). Oklahoma has been more seismically active in the past 8 years in comparison to Kansas, with Oklahoma seismograph stations recording over 9,000 seismic events while Kansas stations recording approximately 3,600 earthquakes (OGS: Earthquake Catalog, KGS: Kansas Earthquakes, 2018). Seismic activity saw an uptick in Oklahoma beginning in 2008, while seismicity in Kansas saw an increase occurring in 2013. Both states have seen a sizeable decrease in earthquakes since waste water disposal restrictions were imposed.

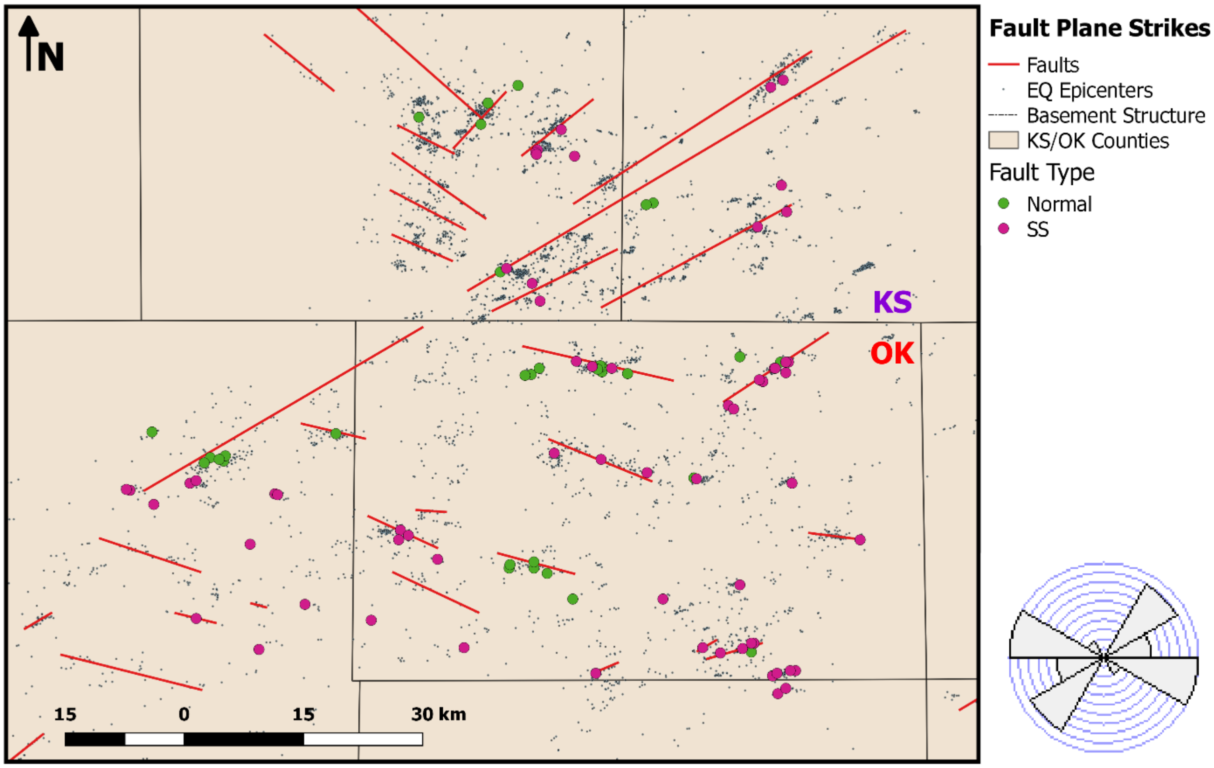

Figure 20: Fault plane lineaments determined from clusters of seismic events and their orientation of propagation**.** The rose diagram in the bottom right corner of the map represents the two dominant fault orientations within the region.

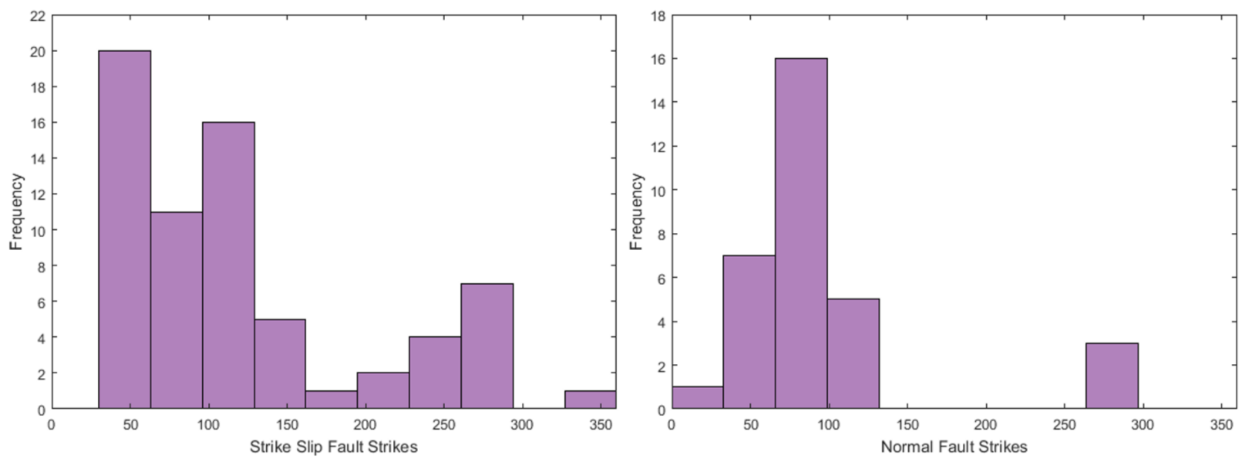

Figure 19: Fault orientations of seismic events with focal mechanism data used to determine the proper slip plane

5.2. Regional Fault Reactivation Potential

Seventy-one of the ninety-nine faults assessed are favorably oriented for reactivation indicated by Q-values of 0.14 or greater (Figure 21). Nine of the ninety-nine faults assessed were unfavorably oriented with Q-values ranging from -0.09 to 0.139 (Figure 21). The remaining 19 fault planes are severely misoriented with Q-values ranging from -1.0 to -0.09 (Figure 21). Faults deemed unfavorably or severely misoriented can only be reactivated by increases in pore fluid pressure or transmission of stress from a nearby fault plane that has recently experienced slip. Seven of the strike-slip faulting events have negative Q-values for each nodal plane orientation. These results suggest that the reactivation of these severely misoriented fault planes could only be induced by an increase in pore fluid pressure.

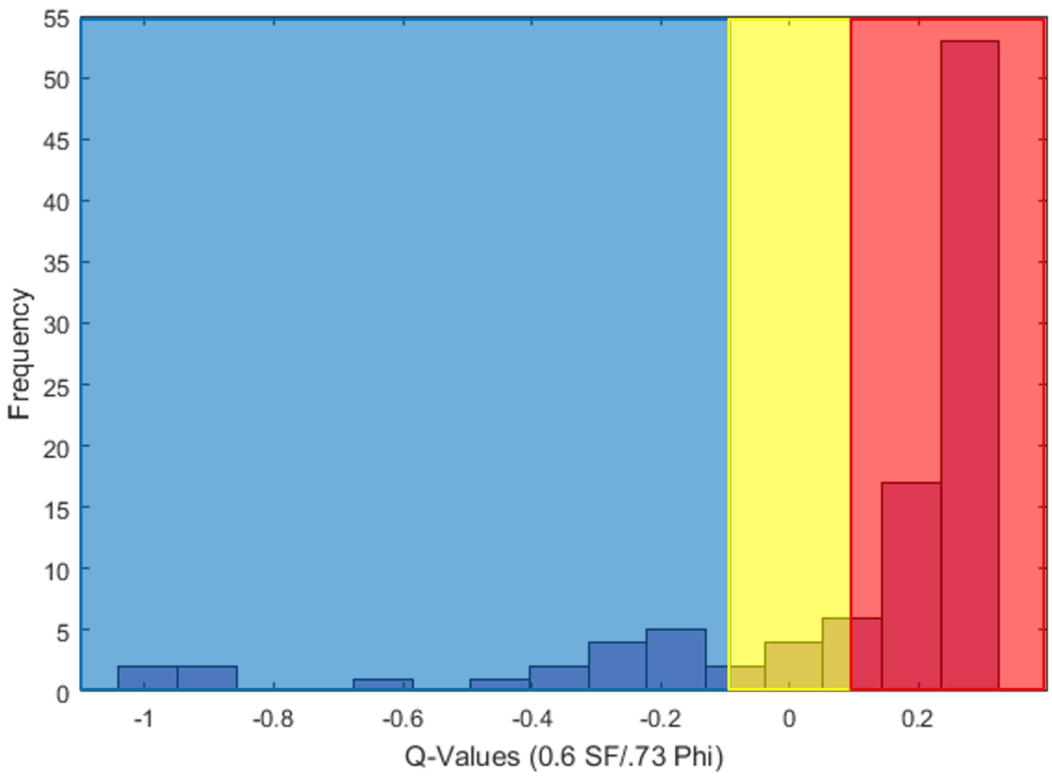

Figure 21: Q-values of all normal and strike slip fault planes within the study region at 0.6 coefficient of static friction and a stress shape ratio of 0.73 phi.

5.3. Computed Pore Fluid Required to Reactivate Faults

The theoretical pore fluid pressures calculated for these seismic events reveal that two-thirds of the fault planes assessed were reactivated with fluid pressure increases of 17 MPa or less. Favorably oriented fault planes required 0.05 MPa to 18.7 MPa based on their computed Q-values and minimum and maximum stresses (Figure 22). Thirty-nine of these favorably oriented faults required 7 MPa or less of fluid pressure for reactivation. Unfavorably oriented faults required 12.4 MPa to 27.19 MPa of excess fluid pressure for reactivation (Figure 23) with an average of 19 MPa. Severely misoriented faults needed fluid pressure increases from 9.1 MPa to 39.7 MPa with an average of 20.1 MPa to initiate reactivation assuming no additional stress transfer from nearby faults and intermediate maximum and minimum principal stress values (Figure 24).

These pore fluid values are theoretical values required for reactivation based on a ϕ of 0.73 and a static coefficient of friction, μ_s, of 0.6. At high normal stresses, 100 MPa or more, the friction is nearly dependent of rock type. At low normal stresses, 50 MPa or less, rock friction is strongly dependent on surface roughness (Byerlee, 1978). Byerlee friction for granite at depth is assumed to be 0.6-0.85. The presence of phyllosilicates along the fault planes could yield lower coefficients of friction which would more easily allow slip of the fault plane at lower effective pore pressures (Collettini et al., 2009). Fault zone restrengthening and frictional healing of strike-slip fault systems is very rapid and can occur within hours to days after an earthquake (Finzi et. al., 2011). While fault healing is possible, it is unlikely to affect results of this study. Many of the fault zones within the study area undergo repeated reactivation that would diminish the effects of fault healing.

Theoretical pore fluid pressures required to reactivate normal faults range from 1.9 MPa to 35.9 MPa assuming pore fluid pressure is the only added pressure and no additional stress transfer from a nearby fault is involved (Figure 25). The theoretical effective pore fluid pressure required to reactivate the strike-slip faults assuming an intermediate stress state range from 0.05 MPa to 28.6 MPa (Figure 26). Both fault regimes require similar effective pore fluid values for reactivation with a clear majority of the fault planes requiring 15 MPa or less for reactivation. The theoretical pore fluid values calculated for each fault can be found in Appendix A-Supplemental Data, Tables 1, 2, and 3.

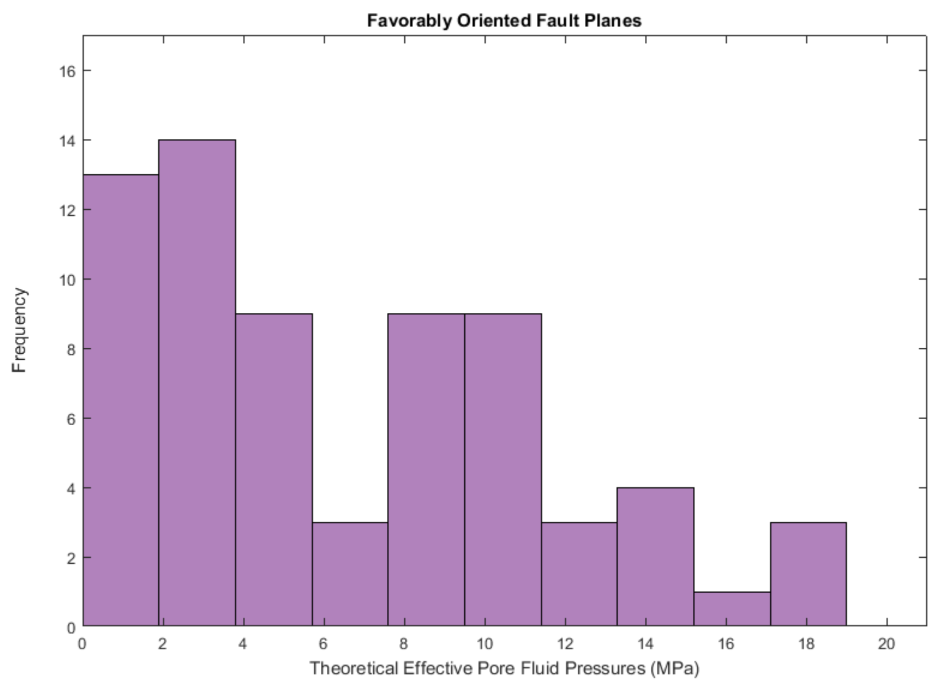

Figure 22: Theoretical pore fluid pressures required for fault reactivation for favorably oriented fault planes. Thirty-six of these faults require less than 5 MPa of effective fluid pressure to reactivate assuming no stress transfer from recently active

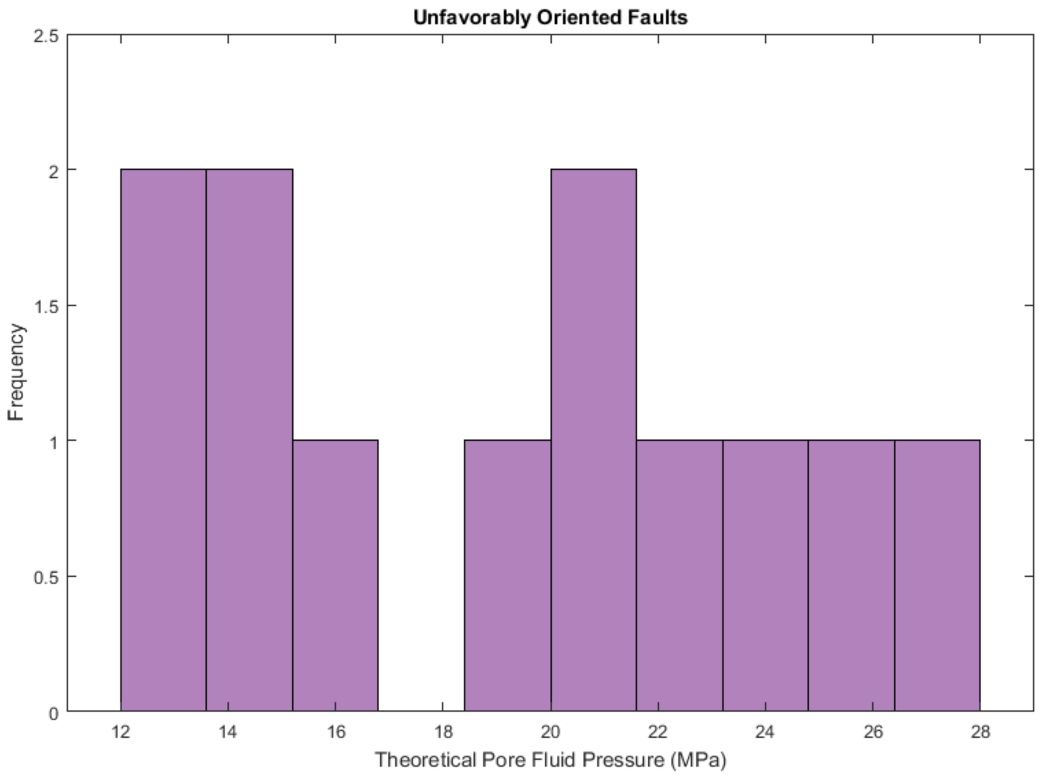

Figure 23: Theoretical effective pore fluid pressures required to reactive unfavorably oriented faults. Effective pore fluid values required change with depth of burial, fault plane orientation with the regional stress tensor, and principal stress magnitudes.

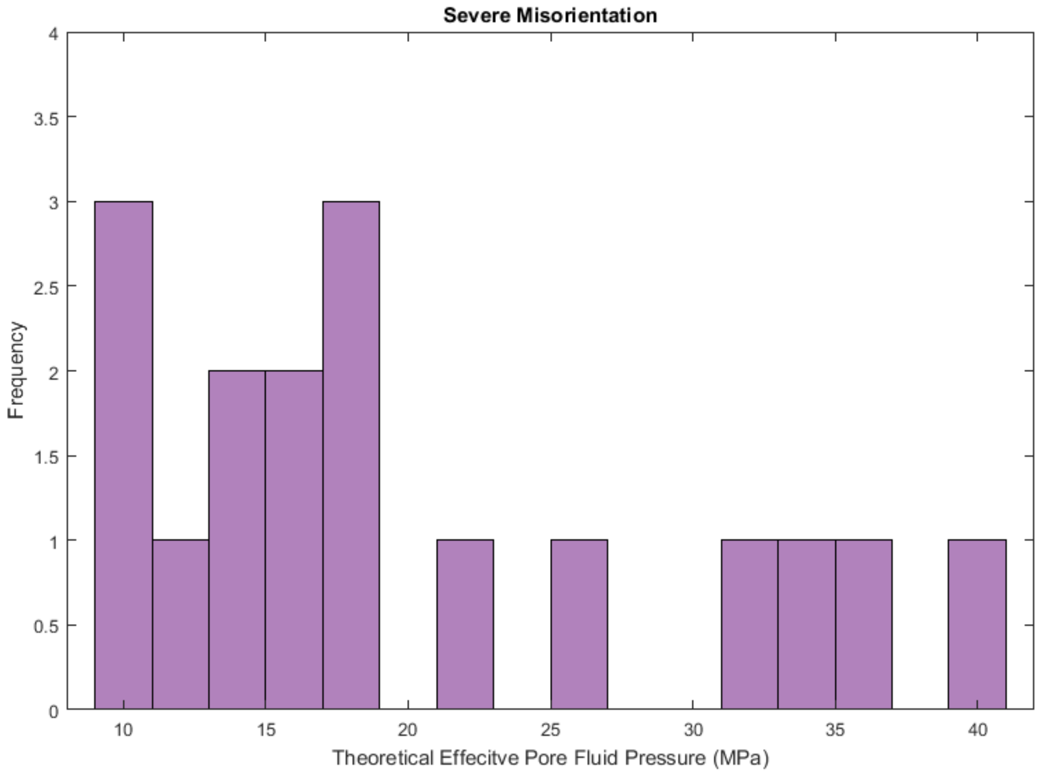

Figure 24: Theoretical effective pore fluid pressures required to reactive severely misoriented faults. Effective pore fluid values required change with depth of burial, fault plane orientation with the regional stress tensor, and principal stress magnitudes.

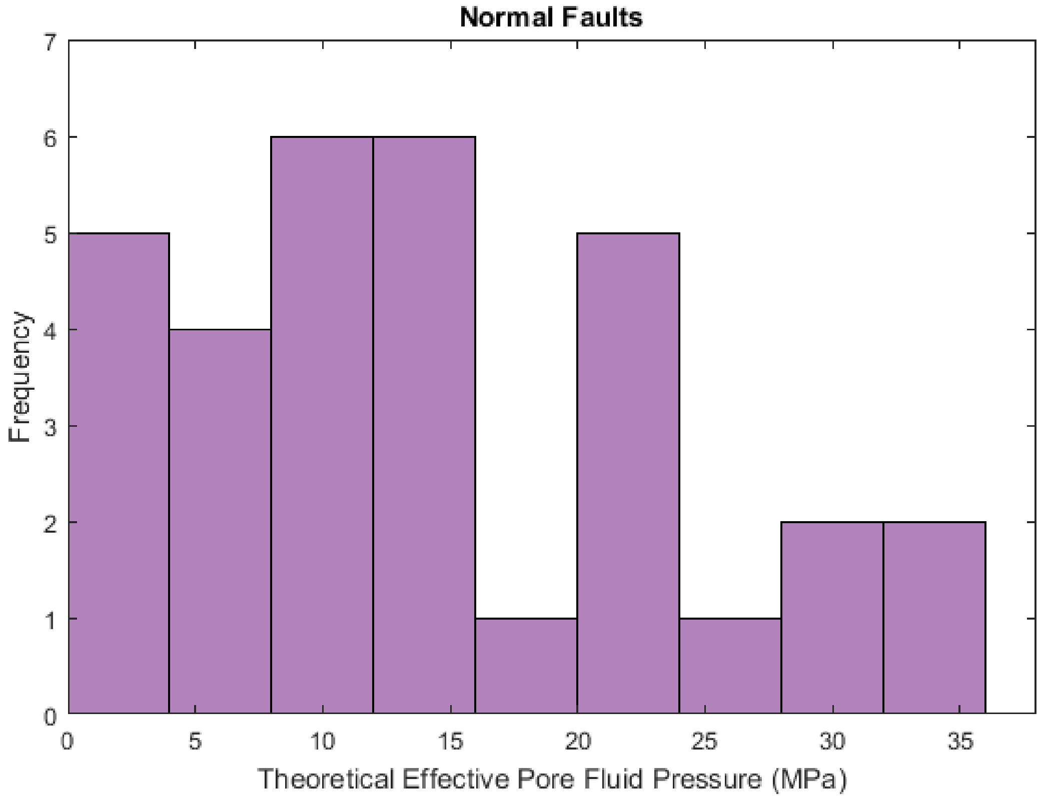

Figure 25: Theoretical pore fluid values required to reactivate normal faults. These values represent purely pore fluid pressure and assume no stress transfer from nearby existing fault planes.

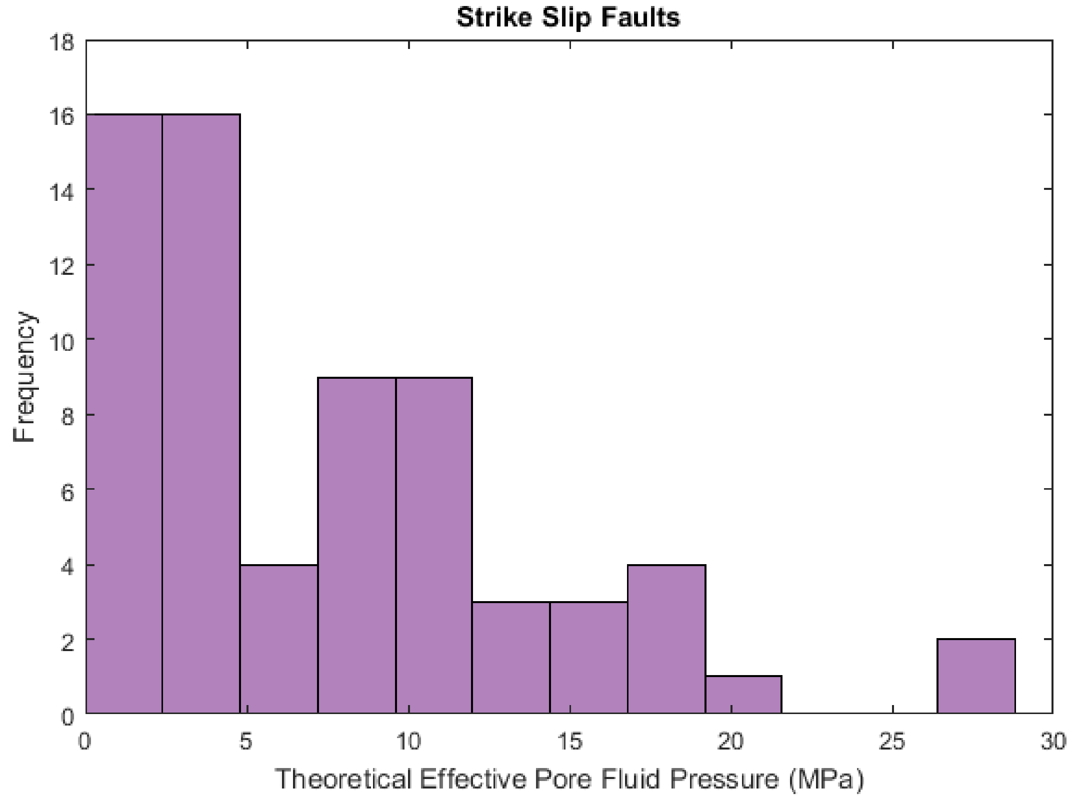

Figure 26: Theoretical pore fluid values required to reactivate strike slip faults. These values represent purely pore fluid pressure and assume no stress transfer from nearby existing fault planes. Intermediate stresses were used to calculate the pore fluid pressure from the stress polygon in Appendix A- Supplementary Data.

5.4. Improving Seismic Imaging of Basement Faults

An accurate understanding of fault geometry is a requirement for understanding their potential for reactivation. It is difficult to track and clearly image faults below the basement contact. Seismic energy is lost in the form of attenuation as the depth of investigation peers deeper into the lithosphere. The loss of both seismic amplitude and spectral bandwidth decreases vertical seismic resolution, which makes clearly imaging or identifying potential fault planes an issue. The initial and boosted frequency spectrum of the data is illustrated in Figure 27. The boosted frequency spectrum ranges from 5-100 Hz (Figure 27).

The goal of this research was to improve the depth of investigation and resolution of a seismic data set where the intended depth of investigation was two disposal zones located in the flat lying sedimentary cover above 1.6 km. The thickest and deeper of the two disposal zones, the Arbuckle Group, extends to a depth of 1.6 km, where it contacts the underlying granitic basement. Three easily identifiable fault planes oriented N030˚ intersect the Mississippian carbonates at a depth of approximately 1.14 km and extend beyond the basement contact within the Anson Bates Field (Figure 29). Their orientations closely resemble the azimuth and near vertical plane geometry expressed by a major basement structure, the Nemaha Ridge, located in the eastern portion of Sumner county. The Nemaha Ridge structure extends approximately 720 km from Omaha, NE to Oklahoma (KGS: Public Information Circular (PIC) 3, 2014), Figure 28). These faults were well documented by Ohl and Raef (2014) and Schwab et al. (2017) and are also in line with structures documented by others regionally (e.g., Bidgoli et al., 2014; Jennings and Bidgoli, 2016; 2017). Their near vertical planes can be tracked to a seismic depth of approximately 3.5 km or 1620 milliseconds(ms) (Figure 31). The fault plane imagery is not finely detailed at these depths, but lineaments can be inferred using the combination of seismic sections and horizontal times slices. Within the Wellington Field, several small fault planes can be identified with similar orientations to those located in Anson field (Figure 31).

Figure 30 is a smoothed similarity horizontal time slice taken at 1.060 ms and a smoothed similarity digitized vertical seismic section across the three near vertical faults of Anson Bates Field. Within Wellington Field to the south, a major lineament oriented approximately 310 degrees can be seen in the northeastern portion of the field (Figure 30 and 31). The fault plane resolution is not great at this depth, but there are undoubtedly subsurface lineaments visible. The NW trending lineament was tracked to a seismic depth of 1620 ms or approximately 3.5 km

(Figure 31). Beyond this depth, the seismic signal becomes too erratic to delineate any further features. Color scales were applied and adjusted to best represent only the lineament feature of interest (Figure 31).

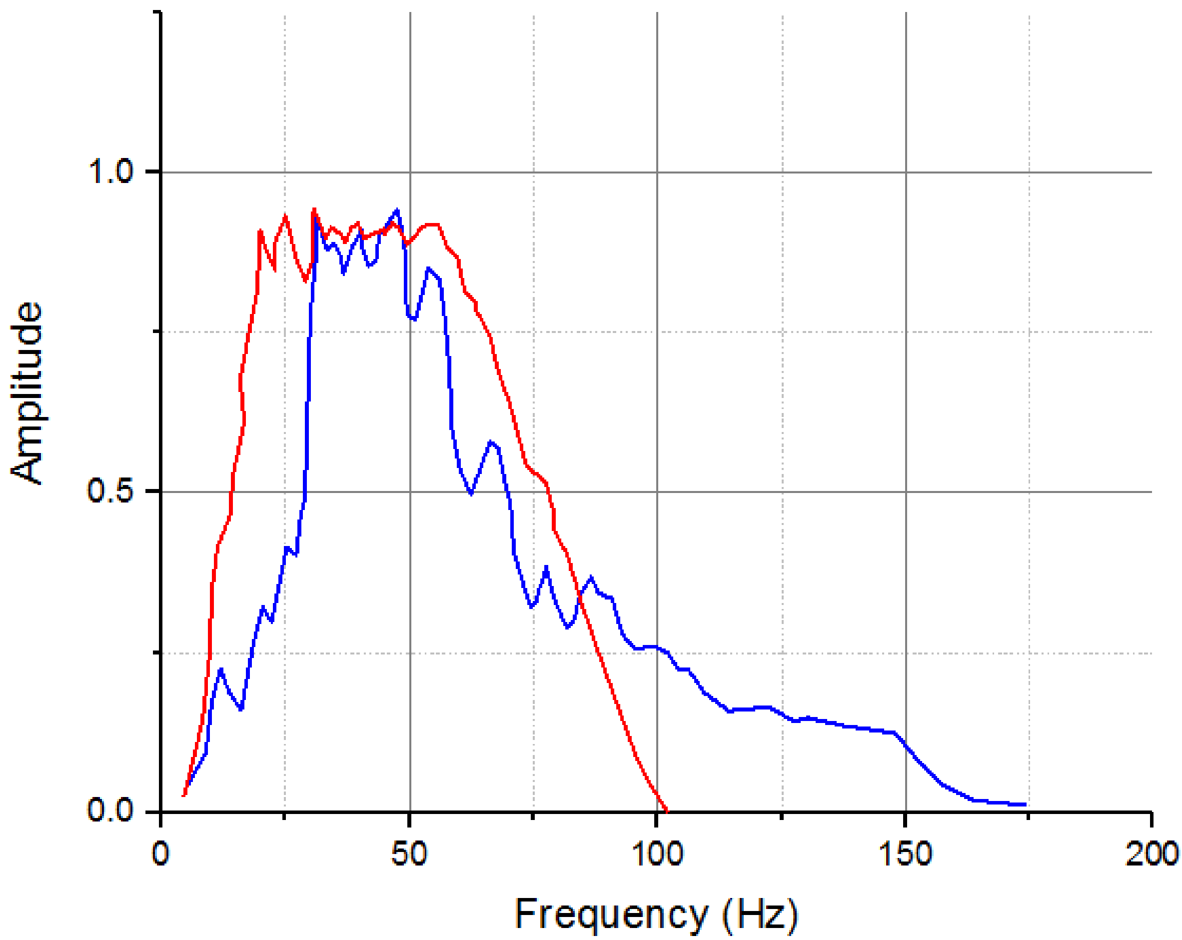

Figure 27: Initial frequency and amplitude spectrum (blue). Boosted amplitude and frequency spectrum (red).

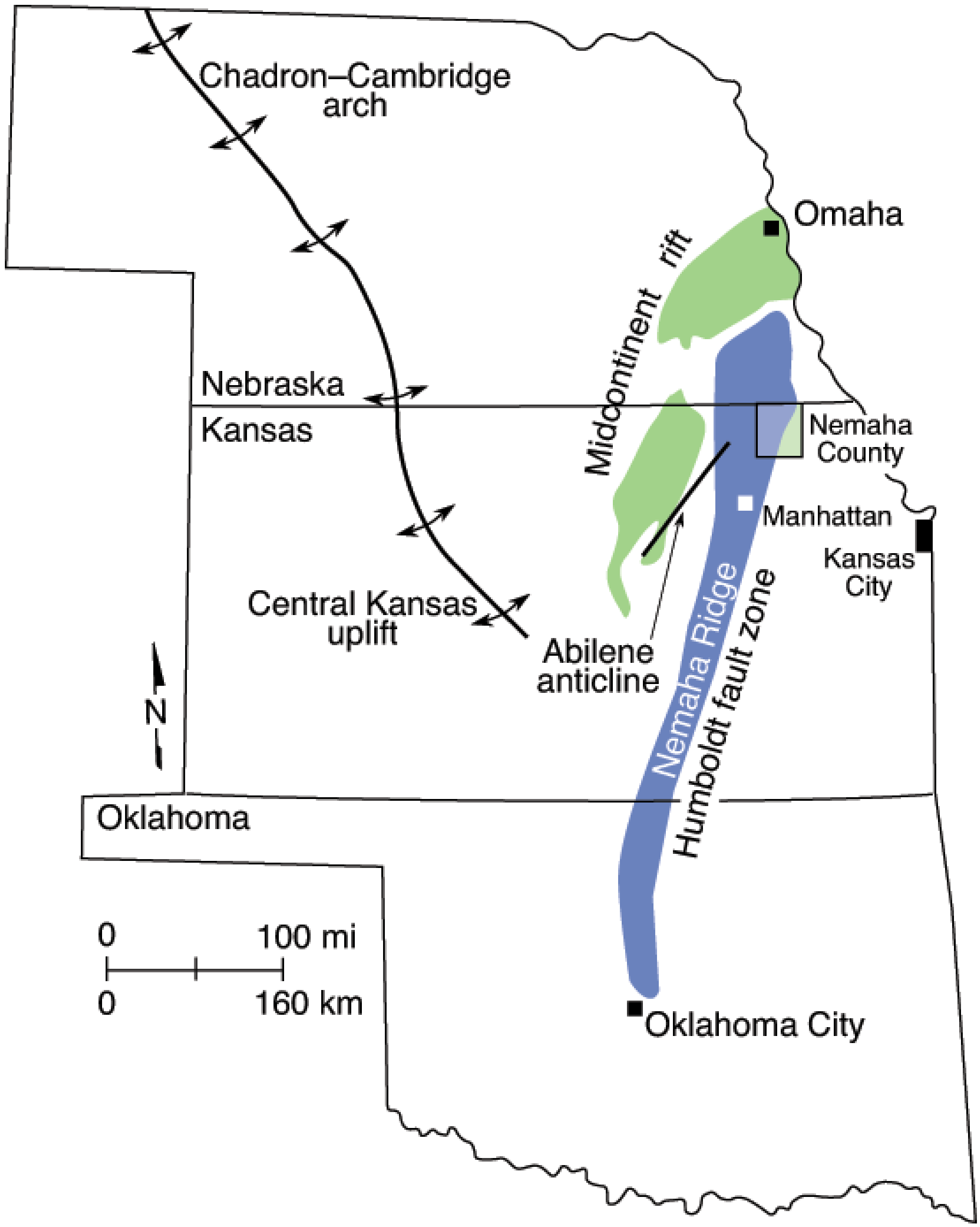

Figure 28: Extent of the Nemaha Ridge structure indicated by the blue region (KGS: Public Information Circular (PIC) 3, 2014).

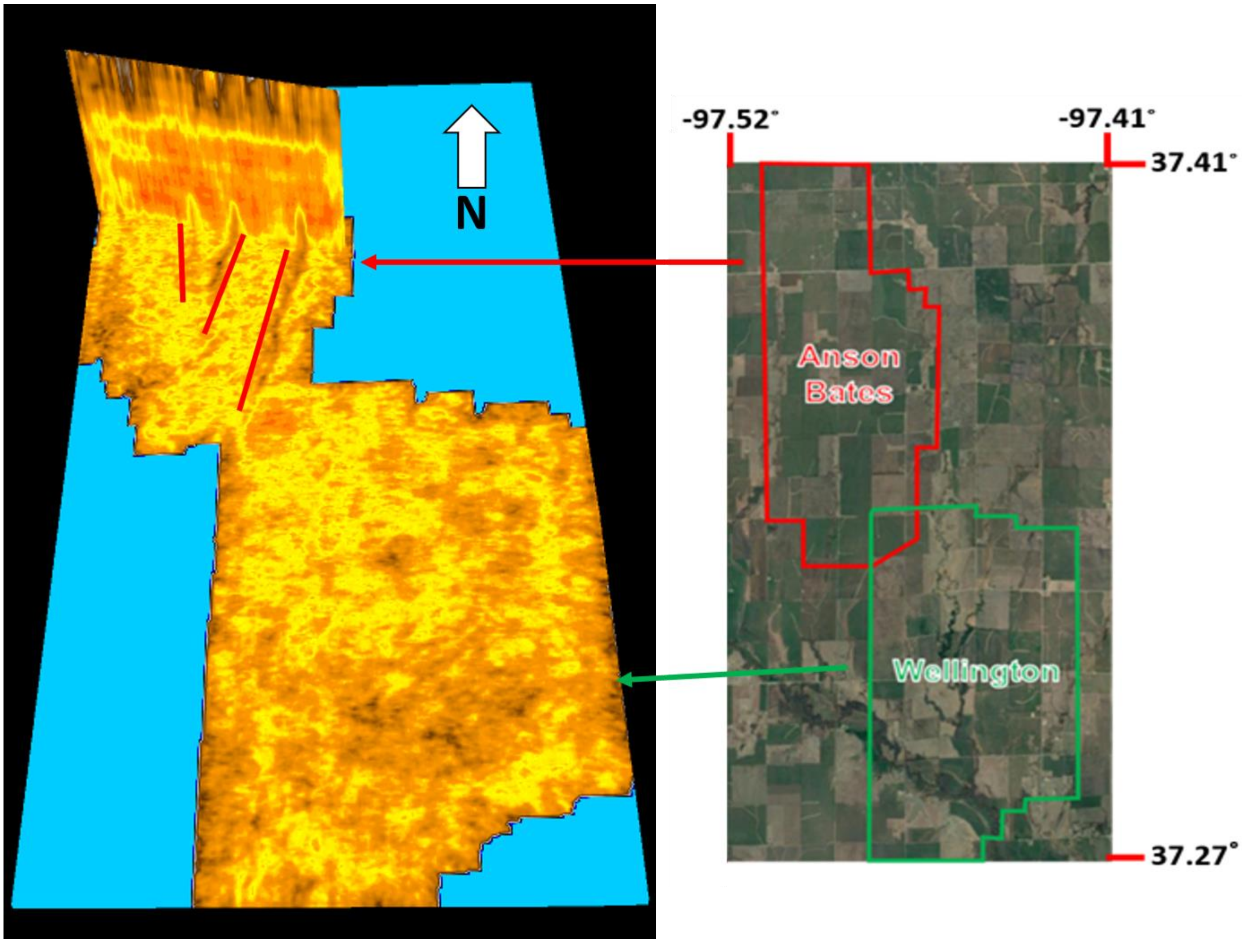

Figure 29: Smoothed similarity horizontal time slice taken at 816 ms. The three near vertical fault features (red lines) are evident on the vertical seismic section. Their fault plane shape can be tracked using the horizontal time slice. No lineaments in Wellington Field are discernible at this depth.

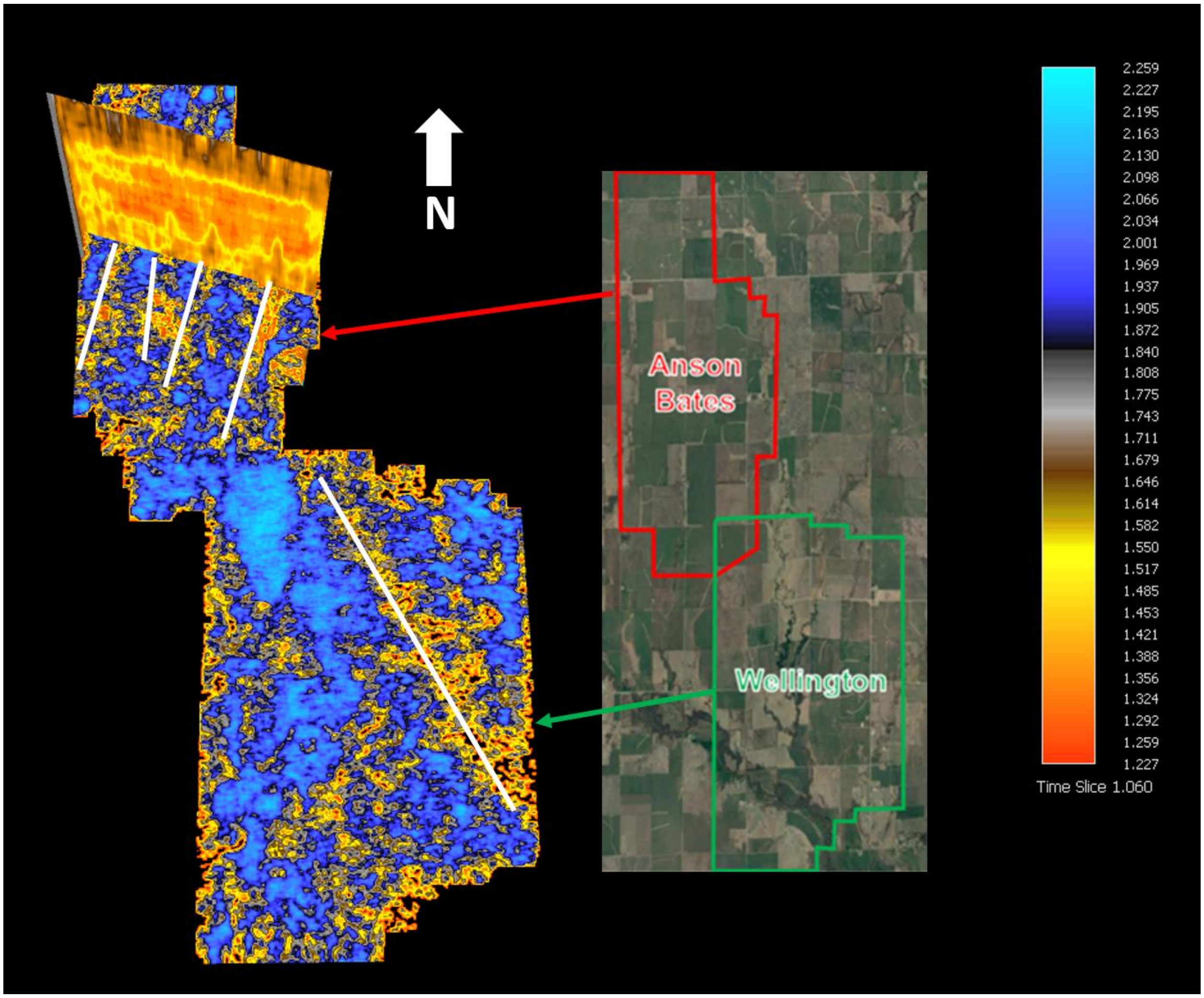

Figure 30: Horizontal time slice taken at 1060 ms. North is to the top of the page. A deeply buried basement lineament striking approximately ~N320˚ (white line) can be seen in the NE portion of Wellington Field. Fault features present within Anson Bates Field (white lines) can be interpreted as well. Fault planes are not clearly defined but can be inferred from the vertical and horizonal seismic images.

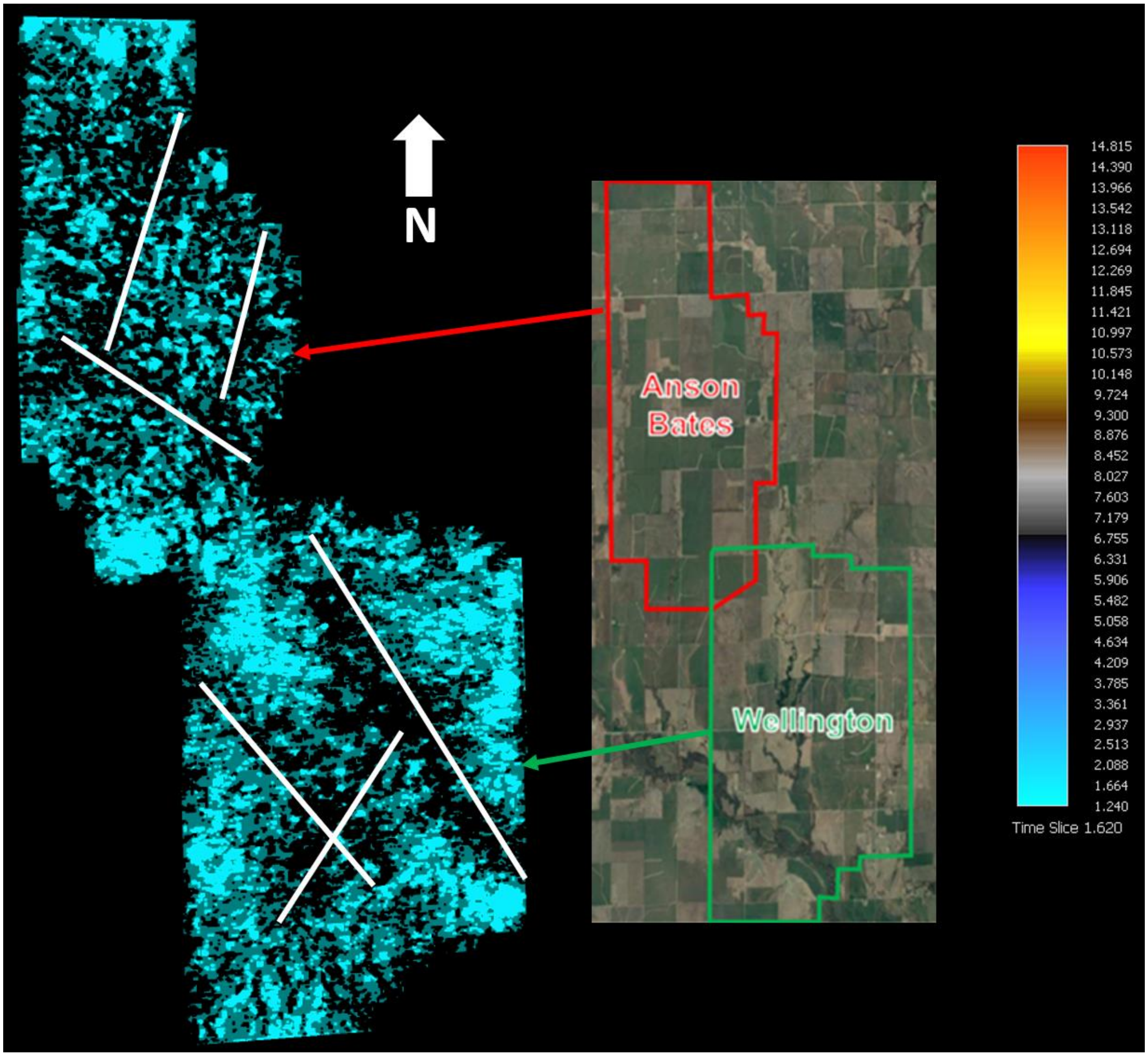

Figure 31: Horizontal time slice taken at 1620 ms which clearly shows three subsurface lineaments within Wellington Field. The imagery is rather crude but expresses the goal of identifying fault features well below the basement contact. The color was adjusted and only select smoothed similarity values were used while others were omitted. The features appear perpendicular to one another. They cross cut Anson Bates Field and intersect two of the three previously described faults that originate in the Mississippian carbonates.

Chapter 6 - Discussion

6.1. Theoretical Effective Pore Fluid Pressure for Fault Reactivation

Considering a friction coefficient, μ_s, of 0.6 and a ϕ of 0.73, seventy-two of ninety-nine faults analyzed were favorably oriented for reactivation under these conditions (Figures 21 and 32). This equates to 72% of the faults under investigation being favorably oriented for reactivation. Their favorable orientation allows induced slip along the fault plane to occur much more easily at lower effective pore fluid pressures or by natural seismicity (Sibson, 1985, Sibson 1990, Leclere and Fabbri, 2013). Favorably oriented fault planes required 0.05 MPa to 18.7 MPa for reactivation with an average of 7 MPa. Schwab et al. (2017) determined that faults striking N020°-N049° may have a moderate to high risk for reactivation with increasing pore fluid pressure. These faults would require a pore fluid pressure increase of at least 1.1 MPa to 7.6 MPa at 1,117 m (Mississippian) and 1.31 MPa to 9.8 MPa at 1,484 m (Arbuckle) to reach failure. Faults at reservoir depths are unlikely to be reactivated given the volume injected. High rates of injection could trigger critically stressed faults (Schwab et. al., 2017). Modeled high pressure triggered earthquakes in Switzerland found average earthquake inducing excess pore fluid pressures of about 10 MPa above hydrostatic pressures at depths from 4-7 km (Terakawa et. al., 2012). The range in excess pore fluid pressures they modeled was from 0.5 MPa to 31.0 MPa (Terakawa et. al., 2012). This is consistent with the research findings of this study.

Seventeen focal mechanisms show evidence of severely misoriented faults, with Q-values from -0.1 to infinity (Tables 1, 2, and 3; Figure 32). This indicates these fault planes are unfavorably oriented regarding the regional stress tensor and only effective pore fluid pressures and/or transmission of stress from a nearby seismic event will reactivate them (Leclere and Fabbri, 2013). Theoretical effective pore pressures required to reactivate these fault planes range in value from 9.1 MPa to 39.7 MPa based on their calculated Q-values, maximum and minimum principal stress magnitudes associated with each fault type, and hydrostatic and lithostatic pressure values related to depth of occurrence (Bethke, 1986; Leclere and Fabbri, 2013). Eleven of the seventeen faults are strike-slip faults with nodal strikes of N139˚-N153˚ and N230˚-N264˚ with dips ranging from 65˚-86˚ (Tables 1, 2, and 3). The seven most severely oriented fault planes are strike-slip faults with Q-values ranging from -0.38 to -0.9905. For the seven severely misoriented strike-slip faults, both nodal planes were determined to be unfavorably oriented indicating that an additional effective stress was needed for their reactivation to occur. Theoretical effective pore pressures required to reactivate these fault planes range in value from 3.7 MPa to 13.6 MPa based on their least negative Q value, strike-slip maximum and minimum principal stress magnitudes, and hydrostatic and lithostatic pressure values related to depth of occurrence (Bethke, 1986; Leclere and Fabbri, 2013). It is important to note both possible nodal planes for these 7 faults were outside the misfit angle criteria of 30˚. Therefore, the least negative Q value of their two nodal planes was chosen.

As pore pressure increases with depth, it trends away from a hydrostatic gradient of 9.8 MPa/km and increases drastically to lithostatic gradient values of 20-25 MPa/km depending on bulk rock density and depth of burial (Bethke,1986, Figure 34). Well logs from the KGS 1-32 indicate that the density of the granitic basement is approximately 2.75 g/cm^3 at a depth of 1.6 km. This equates to a lithostatic gradient of approximately 24 MPa at 5 km depth.

The sharp increase in pore pressure is the result of rock bulk density increases with increasing subsidence and compaction (Bethke, 1986). The increase in the pore pressure gradient results in critically stressed faults as the lithostatic gradient increases to higher values with increasing depth (Bethke, 1986). The result is more easily reactivated faults with relatively small increases in effective pore fluid pressures. A commonly occurring depth trend in the 12,000 plus seismic events is 4-7 km (Figure 33). The steep increase from hydrostatic to lithostatic pore pressures beyond 3.5 km would explain this reoccurring trend of repeated seismic events between 4-7 km depth with relatively small increases in pore fluid pressures.

To help support the case for induced seismicity related to underground injection, ArcGIS geospatial software was harnessed to produce a raster data model of injection wells versus earthquake epicenters in south central Kansas and north central Oklahoma (Figure 35). An ordinary least squares statistical model was applied to the raster data. The resulting negative coefficient for injection wells suggests the probability of an earthquake occurring decreases with increasing distance from the injection site. These results are consistent with conclusions from other studies in the region, which found close association between earthquakes, high-rate injection wells, and the spatial density of injection (Weingarten et al., 2016; Jackson and Bidgoli, 2016).

The depth of wastewater injection regarding its distance from the sedimentary-Proterozoic basement complex has become of interest to induced seismicity researchers (Hincks et. al 2018). Hincks et. al (2018) suggests that restricting injection depths to 200–500 m above basement contact could reduce annual seismic moment release by a factor of 1.4–2.8. Their research found injection depth relative to crystalline basement most strongly correlates with seismic moment release. The joint effects of depth and volume are critical, as injection rate becomes more influential near the basement interface (Hincks et. al., 2008). Injection volumes within Kansas and Oklahoma are rough estimates. Injection volumes were requested and received from the KCC for the years 1987-2015 for Sumner and Harper counties. All years prior to 2015 show that zero barrels of wastewater was injected. This illustrates that wells were not closely monitored until injection was the theoretical culprit of increased seismicity. Therefore, volumes and rates of injection cannot be modeled accurately. The wastewater injection restrictions imposed by the KCC required that all wells injecting into the basement be plugged and abandoned (KCC: UICP, 2015). They did not set a crystalline basement injection distance limitation. In Kansas and Oklahoma, the permeability structure of the Arbuckle Group permits downward fluid migration into crystalline basement (Langenbruch and Zoback, 2013; Shah and Keller, 2017), causing reactivation of optimally oriented strike-slip faults (McNamara et. al, 2015; Fielding et. al., 2017; Schoenball et. al. 2017; Chen et. al., 2017).

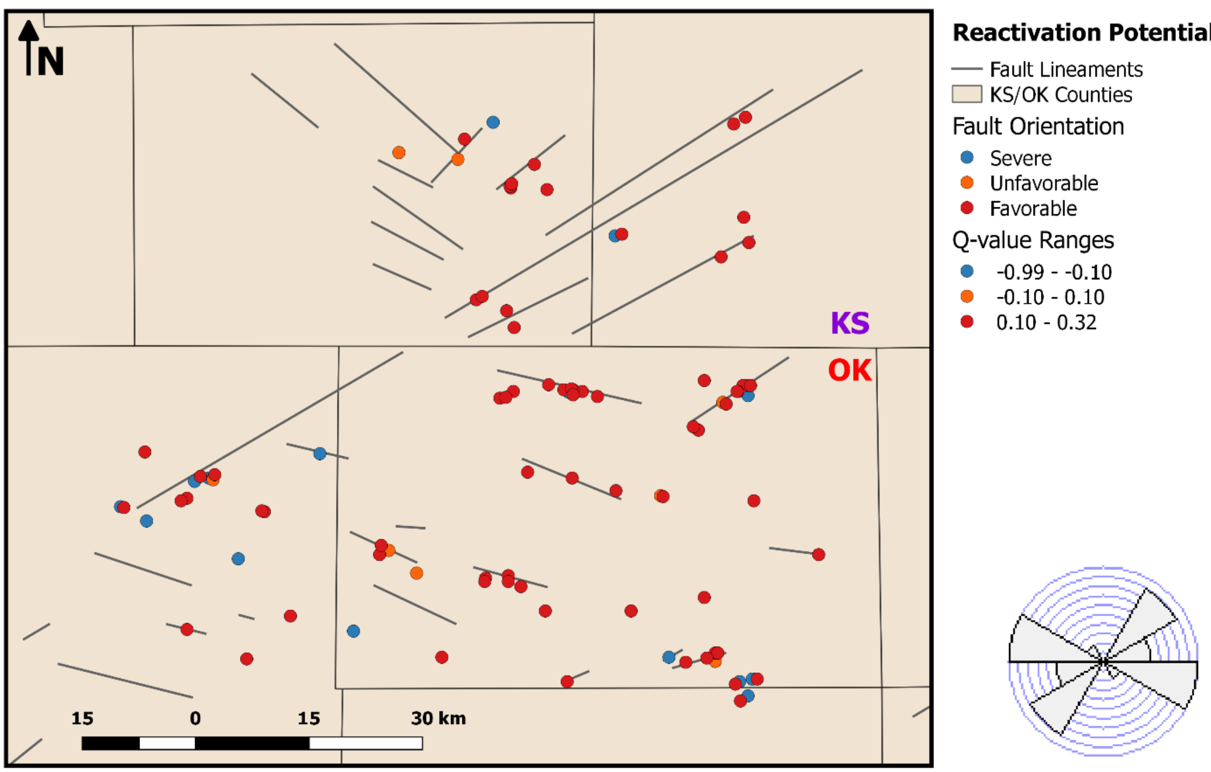

Figure 32: Map of Q-values illustrating the dispersion of faults being assessed and their individual classifications. Red dots indicate that the fault plane is favorably oriented and will reactivate more easily with increasing effective stresses**.** Blue dots represent fault planes that are severely misoriented and will only reactivate with increased effective pore fluid pressures.

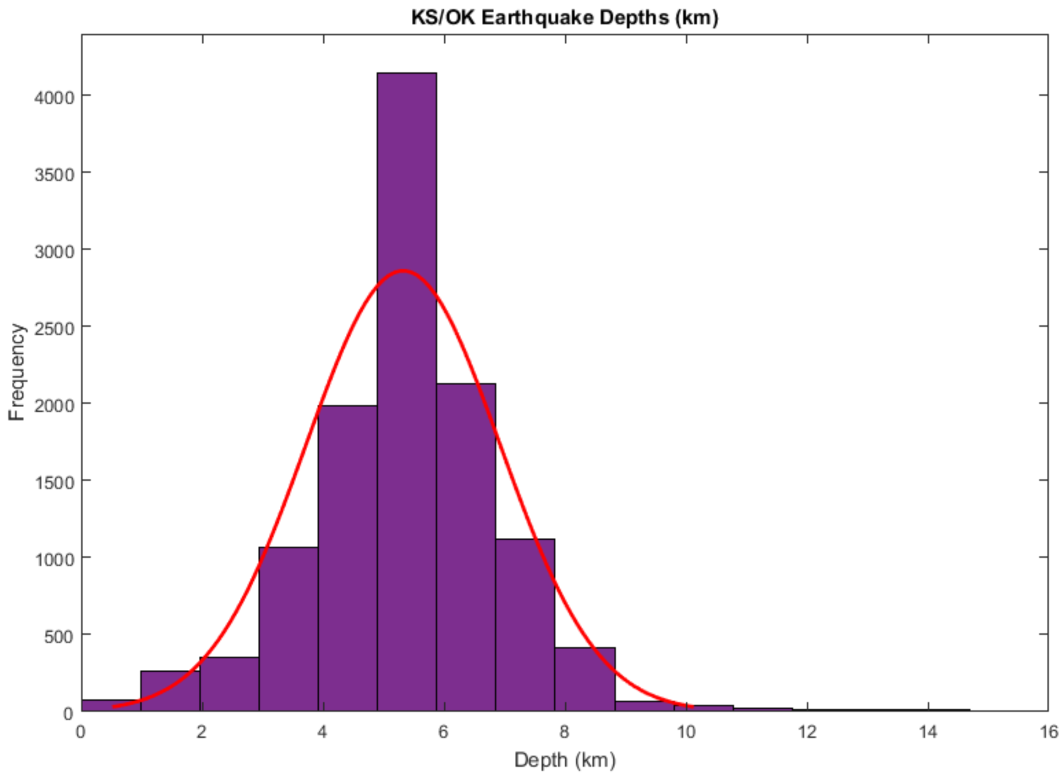

Figure 33: Overall depth distribution of the 12,000 plus earthquakes in Kansas and Oklahoma. A clear trend can be distinguished between 4-7km.

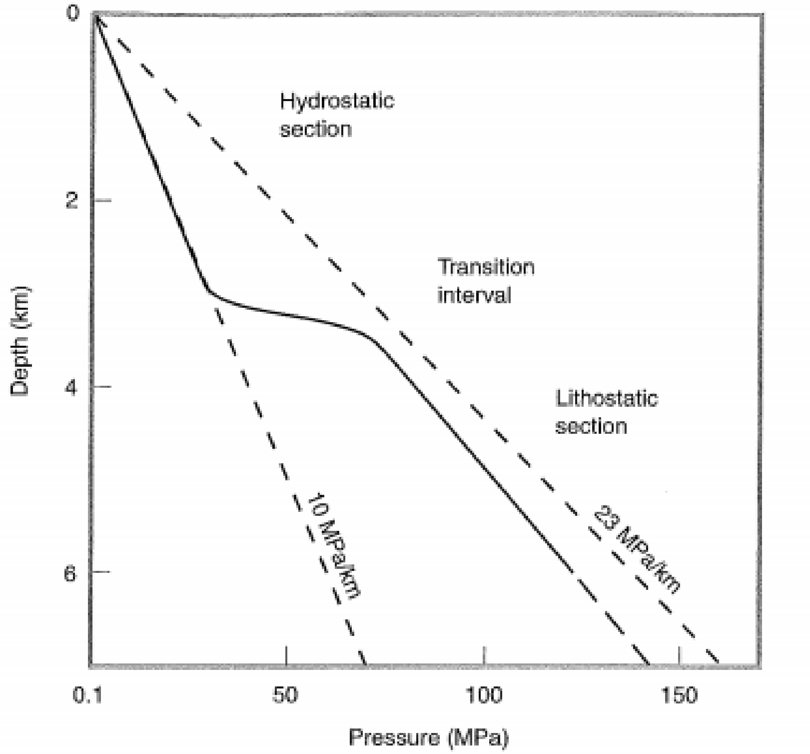

Figure 34: General trend of pore pressure versus depth. At shallow depths, until 3.5 km vertical depth, the pore pressure follows the hydrostatic gradient. Beyond 3.5 km, pore pressure significantly increases and approaches lithostatic pressures (Bethke, 1986).

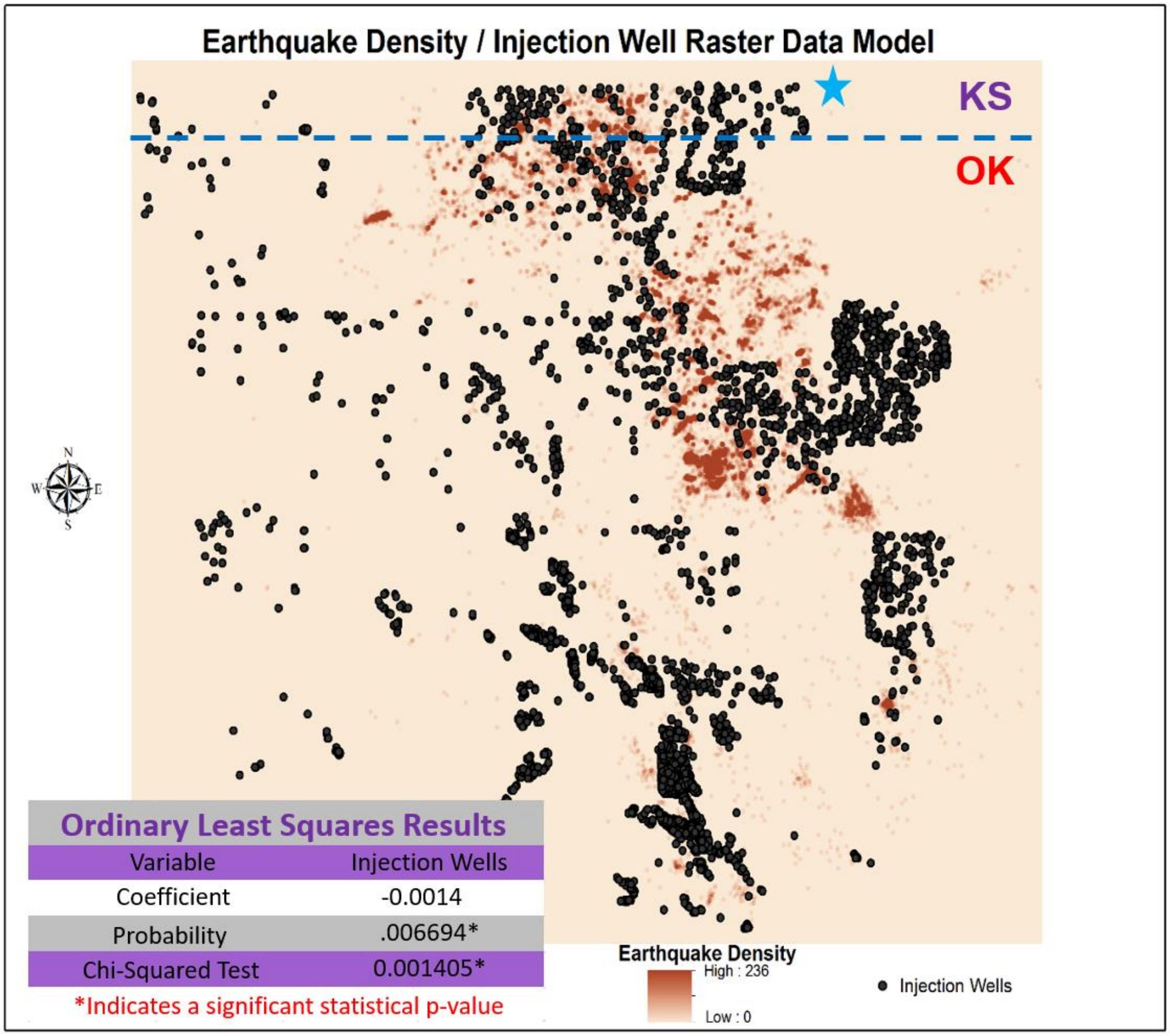

Figure 35: Raster data model generated using the locations of injection wells and earthquake epicenters in northern Oklahoma and southern Kansas.

6.2. Regional Fault Geometry of the Basement

The Proterozoic granitic basement of Kansas and Oklahoma has undergone repeated tectonic events resulting in folding, uplift, and extension (Merriam 1963). This study reveals the presence of two main fault orientations related to well-known basement structures. The presence of these normal and strike-slip faults indicates the past formation of a transtensional basin within the Proterozoic basement complex (Figure 34). The predominance of normal and strike-slip faulting indicates that crustal extension is taking place within the basement complex.

One general fault trend is approximately N030˚ degrees, which I similar to the orientation of the Nemaha Ridge, a feature that extends from Omaha, Nebraska to Oklahoma City, Oklahoma (Figure 28). The other noticeable trend is roughly N300˚ which aligns well with the Central Kansas Uplift, a gentle anticlinal feature. Unfortunately, it is difficult to determine from the small number of focal mechanisms (0.8% of all recorded seismic events) which fault planes are predominately normal or strike-slip faults. Fault lineaments (Figures 19 and 31) measured from the cluster propagation of seismic events agree with regional gravity and magnetic maps produced by the Kansas Geological Survey (KGS: Open File Report 97-72, 1998, Figure 35). Figure 35 depicts the lineaments at the surface of the Proterozoic basement. Most of the earthquakes within the study region occur well below the sedimentary-basement boundary at depths of 4-7 km (Figure 33). Only three of the previously discovered faults within Anson-Bates and Wellington Fields intersect the sedimentary cover and the granitic basement. The lineaments in Wellington Field do not intersect the basement contact. Therefore, they are not depicted in the regional lineaments figure of the Proterozoic basement top.

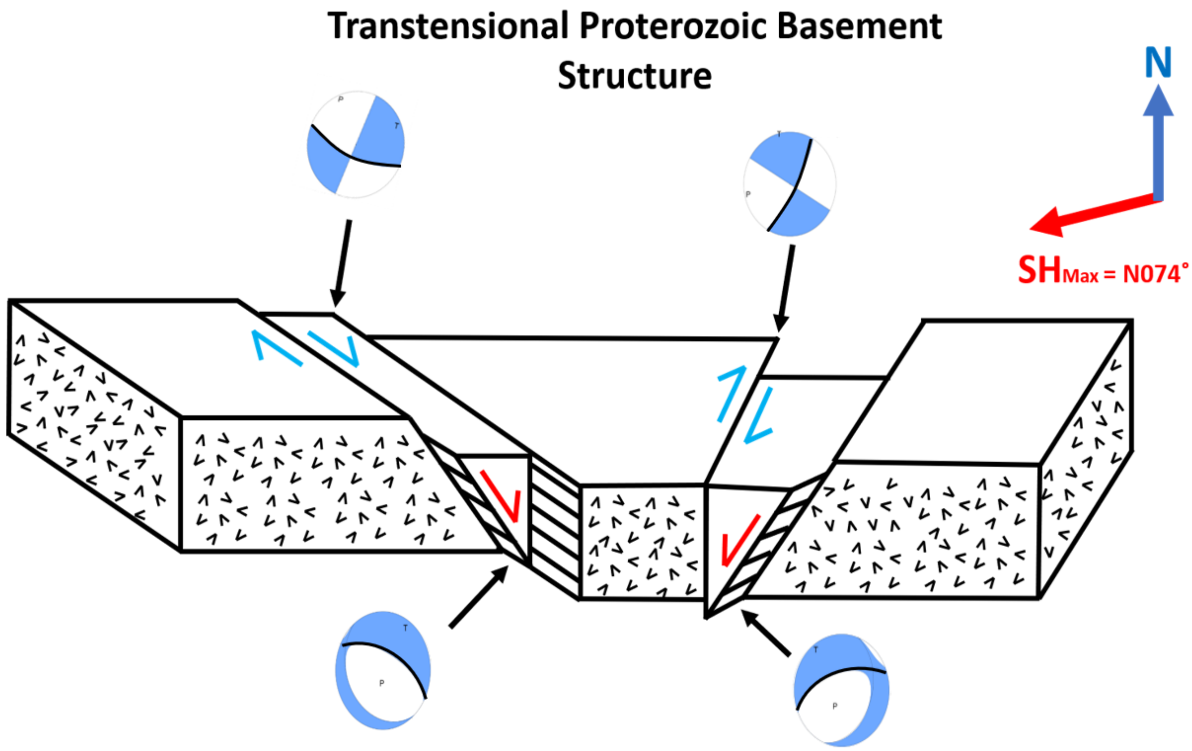

Figure 36: Transtensional basement depiction of the Proterozoic basement

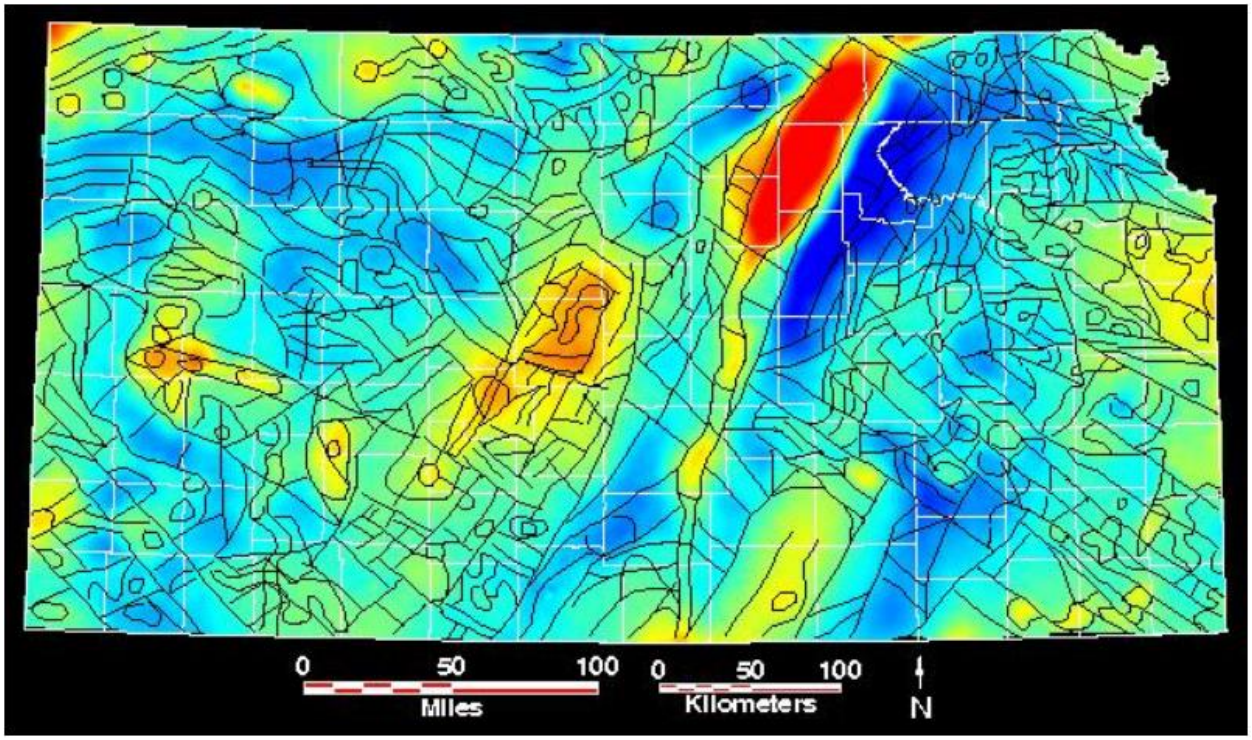

Figure 37: Regional lineations overlaid on a gravity map of Kansas. Two distinct trends of ~N030˚ and ~N300˚ that correlate to earthquake data within the study region can be interpreted. The lineations shown are those present at the top of the Proterozoic basement (KGS: Open File Report 97-72, 1998).

6.3. Seismic Imaging of Basement Lineaments

An accurate understanding of fault geometry is a requirement for understanding fault potential for reactivation. It is difficult to track and clearly image faults beneath the granitic Proterozoic basement contact. Seismic energy is lost in the form of attenuation as the depth of investigation peers deeper into the lithosphere.

Spectral whitening is a technique used on migrated seismic data to overcome frequency attenuation, resulting in improved resolution for a given target zone. In theory, spectral whitening should create a balanced spectrum of amplitudes, although a perfectly balanced spectrum will cause complications, as noise will be accentuated at the low and high ends of the spectrum. To overcome this complication, applying whitening for several specified frequencies within a bandpass filter, and then combining those results, is preferred (Hardy 2002; Mourning, 2016).

Following application of spectral whitening, a suite of spectral analysis tools and filters was applied to the amplitude boosted lower frequency seismic data to asses which revealed the best vertical resolution results in the granitic basement rock. Coherency, similarity, continuity, semblance and covariance are similar and relate to a measure of similarity between several adjacent seismic traces (multi-trace analysis). They convert data into a volume of discontinuity that reveals faults, fractures, and stratigraphic variations (Sacrey and Roden, 2014). Smoothed similarity proved to be most useful when identifying deeply buried lineaments not previously documented. Surface formations of Cretaceous, Tertiary, and Quaternary age mask the underlying structure of the deeper and older beds, structural development of the uplift was concluded before Mesozoic time (Merriam, 1963).

Within Wellington field, several major lineaments were discovered that align with the orientation of a gentle anticlinal structure located in the northwestern portion of Kansas known as the Central Kansas Uplift and the Nemaha Ridge basement structure (KGS: Public Information Circular (PIC) 3, 2014), (Figure 28). The Central Kansas Uplift is the largest positive feature in Kansas, occupying an area of about 14,760 km^2 entirely within the state. The lineament trends approximately N310˚ degrees and coincides with a north and western compression experienced during the Ouachita Orogeny when the Proterozoic basement was uplifted and folded in response to the collision of the South American tectonic plate and the continent of Laurentia (Merriam, 1963).

It is important to identify fault planes which intersect disposal zones and extend into the granitic basement. Porosity and permeability decrease due to subsidence and compaction. Low permeabilities associated with deeply buried granitic rocks hinders fluid migration. Therefore, higher permeability fault planes become conduits through which injection fluids may travel (Sibson, 1990). The presence of these high-pressure fluids along the fault planes allows them to slip more easily. Despite much of Kansas and Oklahoma being flay-lying, the Proterozoic basement has been folded and uplifted numerous times during at least five orogenic pulses. (Merriam, 1963; Johnson, 2008). The lineaments contacting the sedimentary cover within Kansas (Figure 37) are numerous and interconnected.

References

Aber, James S. (2008). Kansas Earthquakes. Emporia State Geology Department. Global Tectonics.

Alt, R. C., II, and Zoback, M.D. (2017). In situ stress and active faulting in Oklahoma. Bulletin of the Seismological Society of America 107(1), doi:10.1785/0120160156.

Angelier, Jacques (1984). Tectonic Analysis of Fault Slip Data Sets. J. of Geophysical Research. Vol. 89. 5835-5848.

Bethke, C.M. (1986). Inverse Hydrologic Analysis of the Distribution and Origin of Gulf Coast Type Pressurized Zones. Journal of Geophysical Research, Vol. 91, no. B6, pp. 6535-6545

Bidgoli, Tandis et al. (2016). Far-Field Reservoir Pressure Increases and Seismicity in South-Central Kansas: GSA Annual Meeting, Denver, Colorado. Presentation and Abstract. 2016.

Bidgoli, T.S., Watney, W.L., Gerlach, P.M., and *Nguyen, M.C., 2014, Episodic reactivation of critically-stressed basement faults in southern Kansas: Implications for wastewater disposal and long-term storage of CO2: Geological Society of America Abstracts with Program, v. 46, p. 317.

Buchanan, Rex. et. al. (2014). Induced Seismicity: The Potential for Triggered Earthquakes in Kansas. Public Information Circular 36. Kansas Geological Survey.

Buchanan, Rex. (2015). Potential Induced Seismicity in the Midcontinent: One State's Experience and Response. Kansas Geological Survey. AAPG. Denver, CO. June 2015.

Burg, Jean-Pierre. (2015). Structural Geology and Tectonics Research Group. ETH Zurich. Geological Institute. Department of Earth Sciences.

Byerlee, J.D. (1978). Friction of Rocks. Pure Applied Geophysics., 116, 615-626.

Cardott, B.J., and Chaplin, J.R., (1993). Guidebook for selected stops in the western Arbuckle Mountains, southern Oklahoma. Oklahoma Geological Survey. Special Publication 93-3, 55 p.

Carr, T., D. F. Merriam, and J. D. Bartley. (2005). Use of relational databases to evaluate regional petroleum accumulation, groundwater flow, and CO2 sequestration in Kansas: AAPG Bulletin, 89, 1670–1627.

Chen, X., N. Nakata, C. Pennington, J. Haffener, J. C. Chang, X. He, Z. Zhan, S. Ni, J. I. Walter., (2017). The Pawnee earthquake as a result of the interplay among injection, faults and foreshocks. Sci. Rep. 7, 4945.

Chopra, Satinder. Kurt Marfurt. (2007). Seismic Curvature Attributes for Mapping Faults/Fractures, and Other Stratigraphic Features. CSEG Recorder Vol. 32 No. 09. November 2007.

Collettini, Cristiano et. al. (2009). Fault zone fabric and fault weakness. Nature. Vol 462. Pg. 907-911. doi:10.1038/nature08585

Delvaux, D. and Sperner, B. (2003). Stress Tensor Inversion from Fault Kinematic Indicators and Focal Mechanism Data: The Tensor Program. In: New Insights into Structural Interpretation and Modelling (D. Nieuwland Ed.). Geological Society, London, Special Publications, 212: 75-100.

Delavaux, Damien (2016). Win-Tensor: Fault-Kinematic Analysis and Tectonic Stress Tensor Inversion.

Dolton, Gordon. Thomas M. Finn. (1989). Petroleum Geology of the Nemaha Uplift, Central Mid-Continent. United States Geological Survey. Open-File Report 88-450D.

Fielding, E. J., S. S. Sangha, D. P. S. Bekaert, S. V. Samsonov, J. C. Chang., (2017). Surface deformation of North-Central Oklahoma related to the 2016 Mw 5.8 Pawnee earthquake from SAR interferometry time series. Seismol. Res. Lett. 88, 971– 982

Finzi, Yaron, Elizabeth H. Hearn, Vladimir Lyakhovsky, Lutz Gross; Fault-zone healing effectiveness and the structural evolution of strike-slip fault systems, Geophysical Journal International, Volume 186, Issue 3, 1 September 2011, Pages 963–970, https://doi.org/10.1111/j.1365-246X.2011.05099.x.

Franseen, Evan K. et. al. (2004). The Geology of Kansas: Arbuckle Group. Kansas Geological Survey. University of Kansas. Bulletin 250. Part 2.

Gerhard, Lee C. (2004). A New Look at an Old Petroleum Province. Kansas Geological Survey, Bulletin 250.

Gibson, David. Michael Spann. Johnathan Turner. (2003). Automatic Fault Detection for 3D Seismic Data. Conference for Digital Image Computing. Macquarie University. CSEG Recorder.

Green, John. (2016). "KCC Imposes New Restrictions on Saltwater Disposal Wells in South-Central Kansas." The Hutchinson News. The Hutchinson News, 09 Aug. 2016. Web. 14 Oct. 2016.

Halls, C. et al. (2000). The Influence of Fluid Pressure in Governing Fracture Geometry and Mineral Textures in the Pneumatolytic Lode Systems of Southwest England. Geoscience in south-west England. Vol. 10. Pg. 058-063.

Hardy, R. (2002). Basic Seismic Processing for Interpreters. Retrieved, from http://www.xsgeo.com/index.html.

Heidbach, Oliver; Rajabi, Mojtaba; Reiter, Karsten; Ziegler, Moritz; WSM Team (2016): World Stress Map Database Release 2016. GFZ Data Services. http://doi.org/10.5880/WSM.2016.001.

Johnson, Kenneth S. (2008). Geologic History of Oklahoma. Oklahoma Geological Survey. Educational Publication 9.

Jackson, C. and Bidgoli, T.S., 2016, Earthquakes in Kansas: A study of brine disposal and injection-induced seismicity: Geological Society of America Abstracts with Programs, v. 48, n. 7, doi: 10.1130/abs/2016AM-285307.

Jennings, J. and Bidgoli, T.S., 2016, Mapping subsurface lineaments and present-day stresses in southern Kansas: A new approach for identifying areas at risk for injection-induced seismicity: Geological Society of America Abstracts with Programs, v. 48, n. 7, doi: 10.1130/abs/2016AM-285652.

Jennings, J. and Bidgoli, T.S., 2017, Identifying Areas at Risk for Injection-Induced Seismicity through Subsurface Analysis: An Example from Southern Kansas: AAPG Datapages/Search and Discovery Article #90291.

Newell, K. D., Watney, W. L., Steeples, D. W., Knapp, R. W., and Cheng, S. W. L., (1989). Suitability of high-resolution seismic method to identifying petroleum reservoirs in Kansas—A geological perspective; in, Geophysics in Kansas, D. W. Steeples, ed.: Kansas Geological Survey, Bulletin 226, p. 9-30.

Kansas Corporation Commission (2016). http://www.kcc.state.ks.us/. Induced Seismicity. October 2016.

Kansas Department of Health and Environment. (2018). KDHE: Underground Injection Control Program. www.kdheks.gov/uic/index/html.

Kansas Geological Survey. (2018). Kansas Earthquakes. http://www.kgs.ku.edu/. October 10, 2016.

Kansas Geological Survey. (2014). Public Information Circular (PIC) 3.

Kansas Geological Survey. (1998). Open File Report 97-72. Gravity and Magnetics. Petroleum Research Section.

Keller, Randy G. (2012). Intraplate Deformation: The Ancestral Rocky Mountains, and the Southern Oklahoma Aulacogen. Oklahoma Geological Survey. Oil and Gas Meeting Presentation March 2012.

Keranen, Katie. (2014). Sharp Increase in Central Oklahoma Seismicity Since 2008 Induced by Massive Wastewater Injection. Science. Vol 345, Issue 6195, pp 448-451. 25 July 2014.

Koester, Edward A. (1935). Geology of the Central Kansas Uplift. Tulsa Geological Society Digest. Volume 4.

Langenbruch, C., M. D. Zoback., (2016). How will induced seismicity in Oklahoma respond to decreased saltwater injection rates? Sci. Adv. 2, e1601542.

Leclere, Henri. Olivier Fabbri. (2013). A New Three-Dimensional Method of Fault Reactivation Analysis. Journal of Structural Geology. Vol. 48. 153-161.

Lueck, Anthony. (2016). Characterizing Two Carbonate Formations for C02-EOR and Carbon Geosequestration: Applicability of Existing Rock Physics Models and Implications for Feasibility of a Time Lapse Monitoring Program in the Wellington Oil Field, Sumner County, Kansas.

Marshak, Stephen. Ben van der Pluijm. (2004). Earth Structure: An Introduction to Structural Geology and Tectonics. Second Edition. WW Norton and Company.

McBee, William. (2003). Nemaha Strike-Slip Fault Zone. Search and Discovery Article #10055.

Merriam. Daniel F. (1963). The Geologic History of Kansas. Kansas Geological Survey Bulletin 162. KGS online version (1998).

Mourning, Rusty. (2014). Seismic attribute analysis of the Mississippian Limestone: Ness County, Kansas. Kansas State University.

Ohl, Derek. Abdelmoneam Raef. (2014). Rock Formation Characterization for Carbon Dioxide Geosequestration: 3D Seismic Amplitude and Coherency Attributes, and Seismic Petrophysical Facies Classification, Wellington and Anson Bates Fields, Kansas, USA. Journal of Applied Geophysics 103. pp. 221-231. 2014.

Oklahoma Geological Survey (2018). Earthquake Catalog. http://www.ou.edu/ogs.html. November 2016.

Peterie, S.L., Miller, R.D., Intfen, J., Bidgoli, T., and Buchanan, R., 2015, A geologically based approach to mitigate potentially induced seismicity in Kansas: SEG Technical Program Expanded Abstracts 2015, p. 4871-4876.

Reynolds, J.M. (2011). An Introduction to Applied and Environmental Geophysics. 2nd Edition. John Willey and Sons.

Rubinstein, Justin. (2016). Effects of Regulation on Induced Seismicity in Southern Kansas. American Geophysical Union Meeting. December 2016.

Sacrey, Deborah, Rocky Roden. (2014). Understanding Attributes and Their Use in the Application of Neural Analysis-Case Histories Both Conventional and Unconventional. Search and Discovery Article #41473.

Schwab, D.R., Bidgoli, T.S., and Taylor, M.H., 2017, Characterizing the potential for injection-induced fault reactivation through subsurface structural mapping and stress field analysis, Wellington Field, Sumner County, Kansas: Journal of Geophysical Research: Solid Earth, v. 122, doi: 10.1002/2017JB014071.

Schoenball, M., W. L. Ellsworth., (2017). Waveform-relocated earthquake catalog for Oklahoma and Southern Kansas illuminates the regional fault network. Seismology. Res. Lett. 88, 1252–1258.

Shah, A.K., G. R. Keller., (2016). Geologic influence on induced seismicity: Constraints from potential field data in Oklahoma. Geophysics. Res. Lett. 44, 152–161.

Sibson, Richard H. (1985). A Note on Fault Reactivation, Journal of Structural Geology. Vol. 7, 751-754.

Sibson, Richard H., (1990). Rupture Nucleation on Unfavorably Oriented Faults. Bulletin of the Seismological Society of America, Vol. 80, No. 6, p. 1580-1604.

Soucek, Charles H., (1959). Structure and Stratigraphy of Sumner County, Kansas Related to Petroleum Accumulation. Kansas State University Ph.D. Dissertation. October 10, 2016.

Terakawa, T. et. al., (2012). High fluid pressure and triggered earthquakes in the enhanced geothermal system in Basel, Switzerland. Journal of Geophysical Research: Solid Earth. Volume 117, Issue B7.

United States Geological Survey (2018). http://earthquake.usgs.gov/earthquakes/search/. Earthquake Database.

Weingarten, et al., (2016). Far-field pressurization likely caused one of the largest injection induced earthquakes by reactivating a large preexisting basement fault structure. AGU publications. Geophysical Research Letters.

Widess, M.B., (1973). How thin is a thin bed? Geophysics. Vol. 38, pg. 1176-1180

World Stress Map (WSM). (2018). www.world-stress-map.org.

Appendix A - Supplementary Data

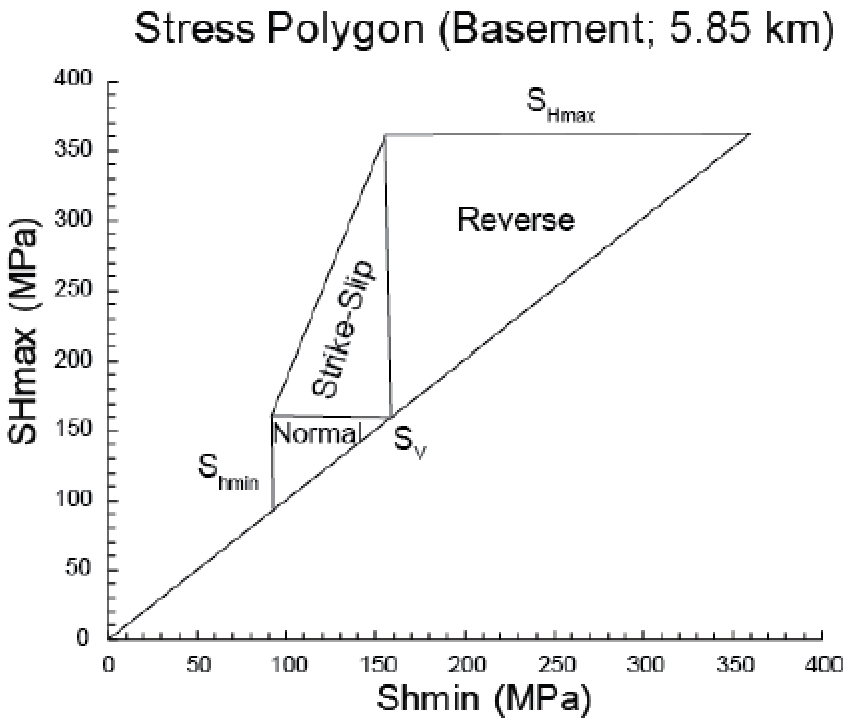

Figure 38: Stress polygon representing the ranges in potential stress present within the Proterozoic basement at a depth of 5.85km. The normal faulting and strike slip stress parameters were utilized to estimate possible stress values present at the average earthquake depth of occurrence (Schwab et al., 2017).

Mag	Lat	Long	Depth (km)	Fault Type	NP Strike	Dip	Q-Value .6 SF	Eff. Pf (MPa)
3.7	37.19	-97.90	3.1	SS	94	65	0.314	0.24
3.6	37.19	-97.90	5.0	SS	180	80	0.251	0.55
3.4	37.19	-97.86	5.0	SS	30	80	0.202	0.56
3.5	36.63	-98.21	6.4	SS	280	80	0.266	0.70
3.9	36.63	-97.65	2.6	SS	65	55	0.308	0.74
3.3	36.6	-97.83	7.2	SS	58	80	0.247	0.79
3.4	36.21	-97.01	7.3	SS	42	80	0.260	0.80
3.9	36.63	-97.67	5.3	SS	68	66	0.311	1.00
3.8	36.76	-98.05	3.7	SS	35	78	0.236	1.22
3.4	37.06	-97.93	5.8	SS	59	62	0.310	1.24
4.2	36.82	-98.29	4.4	SS	285	78	0.265	1.45
3.5	37.22	-97.87	5.0	SS	112	78	0.245	1.65
3.7	36.95	-97.62	5.7	SS	117	78	0.213	1.88
3.5	36.94	-97.83	3.6	Normal	82	62	0.318	1.92
3.5	36.94	-97.80	3.5	Normal	85	60	0.316	2.08
3.9	36.63	-97.66	5.2	SS	64	77	0.251	2.37
4.1	36.95	-97.86	5.0	SS	94	60	0.302	2.46
4.0	36.6	-97.61	5.7	SS	72	77	0.239	2.59
3.4	36.81	-98.36	4.6	SS	44	76	0.269	2.71
3.4	37.15	-97.62	4.6	SS	90	70	0.299	2.72
3.5	36.95	-97.83	2.1	Normal	100	65	0.292	2.81
3.6	37.02	-97.90	7.7	SS	57	65	0.306	2.82
3.9	36.94	-97.91	5.3	Normal	82	56	0.313	2.97
4.9	37.27	-97.62	4.0	SS	290	74	0.249	3.54
3.5	36.94	-97.62	1.6	SS	146	72	-0.440	3.54
4.1	36.95	-97.83	5.0	Normal	82	54	0.307	3.57
3.4	36.95	-97.63	5.0	SS	51	64	0.295	3.62
3.9	36.58	-97.62	4.0	SS	264	82	-0.991	3.71
3.8	36.8	-98.20	4.3	SS	100	64	0.291	3.74
3.4	36.93	-97.64	5.4	SS	105	75	0.195	3.95
3.4	37.26	-97.64	5.0	SS	99	63	0.293	4.00
3.5	36.58	-97.63	5.0	SS	100	70	0.290	4.50
3.3	36.79	-98.33	6.2	SS	235	85	-0.381	4.52
3.4	36.6	-97.63	5.2	SS	358	74	-0.665	4.60
3.6	37.04	-97.91	5.0	SS	63	51	0.288	4.79
3.5	36.75	-98.22	4.6	SS	244	80	-0.957	5.10
4.1	36.82	-97.61	2.8	SS	46	83	0.261	5.17
3.4	36.68	-98.16	5.0	SS	122	73	0.163	5.22
3.7	36.72	-97.90	6.1	Normal	103	56	0.258	5.39
3.8	36.84	-97.83	5.3	SS	121	73	0.174	5.54
3.3	36.68	-97.86	6.6	Normal	275	65	0.299	5.55
3.4	37.05	-97.94	6.2	Normal	61	52	0.290	6.54

Table 1: Theoretical Effective Pore Fluid Values

Mag	Lat	Long	Depth (km)	Fault Type	NP Strike	Dip	Q-Value .6 SF	Eff. Pf (MPa)
3.6	37.19	-97.90	5.0	SS	180	80	0.251	0.550
3.6	37.13	-97.77	5.0	Normal	57	48	0.255	9.120
3.6	36.80	-98.19	5.0	SS	196	90	0.255	10.100
3.4	37.19	-97.90	5.0	SS	44	60	0.264	8.630
4.3	37.25	-97.96	5.0	Normal	81	48	0.276	6.980
3.6	37.04	-97.91	5.0	SS	63	51	0.288	4.790
3.5	36.58	-97.63	5.0	SS	100	70	0.290	4.500
3.4	37.26	-97.64	5.0	SS	99	63	0.293	4.000
3.4	36.95	-97.63	5.0	SS	51	64	0.295	3.620
4.1	36.95	-97.86	5.0	SS	94	60	0.302	2.460
4.1	36.95	-97.83	5.0	Normal	82	54	0.307	3.570
3.4	36.60	-97.63	5.2	SS	358	74	-0.665	4.600
3.9	36.63	-97.66	5.2	SS	64	77	0.251	2.370
3.6	36.96	-97.67	5.2	Normal	105	62	0.269	8.000
3.3	36.94	-97.83	5.3	Normal	47	25	-0.311	34.400
4.3	36.76	-98.05	5.3	SS	127	61	0.052	18.900
3.7	36.87	-98.34	5.3	Normal	84	37	0.140	20.090
3.8	36.84	-97.83	5.3	SS	121	73	0.174	5.540
3.4	36.85	-97.88	5.3	SS	61	85	0.202	18.700
3.9	36.63	-97.67	5.3	SS	68	66	0.311	1.000
3.9	36.94	-97.91	5.3	Normal	82	56	0.313	2.970
3.9	36.87	-98.13	5.4	Normal	82	24	-0.244	35.920
3.4	36.93	-97.64	5.4	SS	105	75	0.195	3.950
4.2	36.48	-98.74	5.4	SS	46	86	0.257	10.500
3.7	36.66	-98.29	5.4	SS	105	61	0.266	9.050
3.7	36.28	-97.51	5.5	SS	142	86	-0.255	7.870
3.3	36.82	-98.29	5.5	SS	115	60	0.195	20.360
4.4	36.72	-97.93	5.6	Normal	87	43	0.219	13.940
4.7	36.75	-98.06	5.6	SS	35	72	0.234	6.800
3.5	36.72	-97.93	5.7	Normal	92	39	0.148	20.900
3.7	36.95	-97.62	5.7	SS	117	78	0.213	1.880
4.0	36.60	-97.61	5.7	SS	72	77	0.239	2.590
3.4	36.83	-97.78	5.8	SS	48	85	0.256	11.400
3.4	37.06	-97.93	5.8	SS	59	62	0.310	1.240
3.7	36.62	-97.66	5.9	Normal	297	65	0.053	12.400
3.7	36.60	-97.63	5.9	SS	86	87	0.186	14.300
3.7	37.11	-97.65	5.9	SS	276	89	0.243	10.340
3.7	36.95	-97.90	5.9	Normal	71	45	0.254	10.690
3.7	36.72	-97.90	6.1	Normal	103	56	0.258	5.390
3.3	36.79	-98.33	6.2	SS	235	85	-0.381	4.520

Table 2: Theoretical Effective Pore Fluid Values Continued

Mag	Lat	Long	Depth (km)	Fault Type	NP Strike	Dip	Q-Value .6 SF	Eff. Pf (MPa)
3.6	36.73	-98.01	6.2	SS	128	57	0.006	28.60
3.4	37.05	-97.94	6.2	Normal	61	52	0.290	6.54
3.6	36.66	-98.09	6.4	SS	140	65	-0.234	16.76
3.8	37.23	-98.03	6.4	Normal	103	37	0.047	28.90
3.5	36.63	-98.21	6.4	SS	280	80	0.266	0.70
3.3	36.75	-97.53	6.6	SS	110	85	0.249	14.58
3.4	36.90	-97.68	6.6	SS	100	55	0.267	10.91
3.3	36.68	-97.86	6.6	Normal	275	65	0.299	5.55
3.8	36.28	-97.51	6.7	SS	135	85	-0.043	12.83
3.4	36.95	-97.62	7.0	Normal	288	50	0.172	14.17
3.3	36.60	-97.83	7.2	SS	58	80	0.247	0.79
3.4	36.21	-97.01	7.3	SS	42	80	0.260	0.80
3.3	36.62	-97.69	7.4	SS	63	85	0.190	18.60
3.6	36.95	-97.62	7.6	SS	139	72	-0.170	9.22
3.6	37.02	-97.90	7.7	SS	57	65	0.306	2.82

Table 3: Theoretical Effective Pore Fluid Values Continued